Research Square

Preprints are preliminary reports that have not undergone peer review.
They should not be considered conclusive, used to inform clinical practice,
or referenced by the media as validated information.

The role of natural and forced variability in shaping atlantification of the Arctic Ocean

Igor Polyakov

ivpolyakov@alaska.edu

University of Alaska Fairbanks

Andrey Pnyushkov

UAF

Thomas Ballinger

University of Alaska Fairbanks https://orcid.org/0000-0002-8722-1927

Michael Lundberg

UAF

Sergey Molodtsov

UAF

Milena Veneziani

LANL

Physical Sciences - Article

Keywords:

Posted Date: June 1st, 2026

DOI: https://doi.org/10.21203/rs.3.rs-9519729/v1

License: This work is licensed under a Creative Commons Attribution 4.0 International License.
Read Full License

Additional Declarations: There is **NO** Competing Interest.

The role of natural and forced variability in shaping atlantification of the Arctic Ocean

Igor V. Polyakov[1*], Andrey V. Pnyushkov[2], Thomas J. Ballinger[2], Michael Lundberg[1], Sergey Molodtsov[2], Milena Veneziani[3]

1 International Arctic Research Center and College of Natural Science and Mathematics, University of Alaska Fairbanks, Fairbanks, USA

2 International Arctic Research Center, University of Alaska Fairbanks, Fairbanks, USA

3 Los Alamos National Laboratory, Los Alamos, USA

Type of the manuscript: Original research. Figures/Tables: 5/0. Length: 3162 words. 56 (32 in main text plus 24 in Supplement) references.

*Corresponding author: Igor V. Polyakov, 907-474-2686, ivpolyakov@alaska.edu

Abstract

The Arctic Ocean is undergoing atlantification, marked by increased influence of warm, saline Atlantic Water (AW) on stratification and sea ice[7-9]. Observations from 1948–2025 reveal that this trend is not monotonic: since 2007–2008, AW cooling has occurred, with partial re-stratification of the Eurasian Basin emerging in the 2020s. Using an Arctic-focused Earth System Model, we show that externally forced trends dominate sea-ice loss, whereas oceanic trends remain within the range of internal variability. Internal variability modulates atlantification events, including recent AW cooling and Eurasian Basin re-stratification, but its influence diminishes with timescale as externally forced variability prevails at decadal and longer scales. Together, these results highlight a nonlinear, state-dependent Arctic system in which variability modulates atlantification against ongoing climate forcing.

One-Sentence Summary: The Arctic Ocean is warming and losing sea ice due to climate change, but natural fluctuations can temporarily slow or reverse these changes.

Introduction

The Arctic is one of the fastest-warming regions of the Earth system, amplifying global climate change through powerful feedbacks associated with snow and sea-ice loss[4-6]. Since the late 1970s, Arctic surface air temperatures have risen at nearly four times the global mean rate, accompanied by dramatic declines in sea-ice extent, area and volume across all seasons[7,8]. These changes, unprecedented in the instrumental record (*9*), reflect tight coupling between atmosphere, ocean and sea ice (**Extended Data Fig. 1**), which has strengthened as thinning ice and enhanced upper-ocean circulation promote greater exchanges of heat and freshwater[1-3]. A defining manifestation of this transformation is atlantification (**Fig. 1**): the increasing penetration of warm, saline Atlantic Water (AW) into the Arctic Ocean, leading to intermediate-layer warming, weakened stratification and enhanced upward ocean heat fluxes, particularly in the Eurasian Basin (EB; **Fig. 1b-e**, *11,12*).

Arctic climate change results from the combined influence of intrinsic (internal or natural) variability and extrinsic (forced) variability arising from natural or anthropogenic external forcing. Superimposed on the long-term warming trend is pronounced variability spanning interannual to multidecadal timescales (e.g., *13-16*), linked to large-scale circulation modes such as the Arctic Oscillation, North Atlantic Oscillation, and Atlantic Multidecadal Oscillation (*17-19*). Anthropogenic radiative forcing, dominated by increasing greenhouse gas concentrations, has been identified as the primary driver of long-term Arctic warming, with its magnitude far exceeding that of natural radiative forcing since the preindustrial era (*6, 20*). At the same time, internal variability and external forcing modulate the timing and regional expression of sea-ice and ocean changes (*21,22*). Sparse observations and model limitations hinder clear separation of externally forced trends from intrinsic variability, particularly for subsurface ocean processes and emerging feedbacks (*23,24*). Here, we integrate observations and Arctic-focused Earth System Model (E3SM-Arctic) simulations to disentangle how internal variability and external forcing regulate atlantification and shape divergent Arctic Ocean basin trajectories across timescales.

Contrasting regional evolution of Arctic Ocean freshwater, heat, and sea ice

Observations reveal contrasting trajectories of upper-ocean stratification in the Arctic's two main basins (**Fig. 2a–c, Extended Data Fig. 2**). Decomposition of freshwater content

(FWC) shows that both the sign and magnitude of trends depend strongly on timing of the dominant mode of variability (**Fig. 3**). Over 1948–2025, the trend indicates modest freshwater loss in the EB and a strong opposing tendency toward freshwater gain in the AB. In contrast, the multidecadal mode (periods longer than 32 years) evolves largely in phase between the two basins and contributed to the freshening since the late 1990s. During the 2020s, the basins diverged again, with renewed freshening and re-stratification in the EB and freshwater loss accompanied by increased salinification in the AB. These recent EB re-stratification tendencies partially offset the long-term atlantification signal, indicating a moderation of atlantification-related impacts in that basin.

The E3SM-Arctic simulations reproduce many of the observed features of Arctic atlantification (**Fig. 2d–f, j–l, p–r**). Ensemble-mean results closely track observed pan-Arctic and basin-scale FWC and sea ice area (SIA) variability over 1950–2014, lending confidence to the model's representation of large-scale freshwater redistribution and ice–ocean coupling. In particular, the model successfully captures the differences in regional FWC trends, a critical benchmark for simulating atlantification.

In contrast to FWC, AW core temperature (AWCT) exhibits coherent variability across the basins (**Fig. 2g–i**), with a significant positive lagged correlation between the EB and AB over 1948–2025 ($R = 0.62$ $p < 0.001$) and the EB leading by 11–12 years. Pan-Arctic AWCT is also strongly correlated with FWC ($R = 0.77$, $p < 0.001$) and lead them by ~14 years. These relationships are consistent with the mooring records from the eastern EB (**Fig. 1**). Both historical and control E3SM-Arctic simulations show pronounced AWCT and FWC variability across decadal to multidecadal timescales (**Extended Data Fig. 3**), consistent with observed low-frequency Arctic climate variability (*13,14*), but the simulated pan-Arctic and regional AWCT trends are substantially weaker than observed (**Fig. 2j-l**). While AW temperatures increased in both basins through 2007–2008, more recent observations indicate a clear decline in AWCT in both the EB and AB. Given the lagged relationship between AWCT and FWC, recent changes in both variables are highly consistent.

Nevertheless, contrasting stratification states in the two basins imply that similar AW temperature anomalies can have markedly different impacts on surface conditions and sea ice, as reflected in September SIA trends (**Fig. 2m–o, Extended Data Fig. 4**). During the early satellite era, the AB experienced a more rapid late-summer ice decline, followed by

a pronounced hiatus after ~2007 with weak, non-significant trends thereafter (**Extended Data Fig. 4b**). In contrast, September SIA in the EB has continued to decline into the most recent decade (**Fig. 2m–o, Extended Data Fig. 4**). The persistence of EB sea ice loss during the 2020s, despite recent AW cooling and partial re-stratification, indicates sustained oceanic forcing, likely reflecting the cumulative effects of earlier halocline weakening and upward ocean heat flux, evident as deep (>120 m) wintertime ventilation in the EB mooring record (**Fig. 1**). Notably, these ice–ocean changes are not mirrored by Arctic surface air temperature variability, a key component of atmospheric forcing (**Extended Data Fig. 1**), suggesting an important role for internal ice–ocean variability in shaping sea ice and ocean evolution.

Emergence of forced trends versus modes of variability

Together, these results motivate a closer examination of the modal structure of upper-ocean and sea-ice variability, with particular emphasis on the relative magnitudes of interannual (5–10 yr), decadal (15–30 yr), and multidecadal (40–60 yr) fluctuations and the long-term trend. The modal decomposition of the E3SM-Arctic results reveals clear differences in how variability and long-term change contribute to FWC, AWCT, and SIA, as quantified by the standard deviations of each component (**Fig. 3**).

For SIA, the long-term trend dominates the variance budget across all regions, indicating that externally forced change governs SIA evolution at the longest timescales (**Fig. 3g-i**). This dominance is most pronounced at the pan-Arctic scale, where the trend's standard deviation (0.31) is 2.4 times larger than the combined variability across frequency bands evident in the record (0.13), indicating that sea-ice loss is dominated by low-frequency change captured by the long-term trend rather than variability resolved in the record.

In contrast, the balance between variability and trend differs markedly between the AB and EB for FWC and AWCT. In the AB (**Fig. 3b,e**), the SD of the trend exceeds that of the combined interannual, decadal, and multidecadal variability for both variables, indicating that long-term change dominates the variance and largely controls basin-scale evolution. Variability in the AB therefore plays an important but secondary role, superimposed on a strong underlying trend. The EB exhibits the opposite behavior (**Fig. 3c,f**). There, low-frequency variability accounts for a substantial—and in some cases dominant—fraction of the total variance. For FWC, the combined SD of the three

variability bands exceeds that of the long-term trend, while for AWCT the two contributions are comparable. This contrast indicates that variability exerts a disproportionately strong influence on EB hydrographic evolution, modulating and sometimes obscuring long-term trends.

Overall, these basin-dependent differences demonstrate that while SIA changes are overwhelmingly trend-dominated across the Arctic, FWC and AWCT respond very differently in the AB and EB. Trends explain more of the total variance than variability in the AB, whereas in the EB, variability plays an equal or larger role than the long-term trend, highlighting fundamentally different controls on Arctic change between the two basins.

The temporal evolution of pan-Arctic FWC, AWCT, and SIA is closely linked to greenhouse radiative forcing, with correlations ranging from $R = 0.58$ to $R = 0.91$ (**Fig. 2a,g,m**). Nevertheless, **Fig. 3** shows that recent departures from monotonic behavior—such as the sea-ice hiatus, AWCT cooling, and partial re-stratification in the EB—arise from interactions between variability modes. For example, in the EB, variability-driven freshwater gains in the 2020s partially offset the long-term change, with the decadal mode accounting for 82% of the total variability contribution. Thus, while the trend reflects the background state, interannual-to-multidecadal variability modulates the timing, magnitude, and even the sign of observed regional changes on societally-relevant timescales.

Relative magnitude of natural and forced variability

Extended Data Figure 3 quantifies the relative importance of natural and forced variability by comparing standard deviations of simulated time series from the control run (natural variability) and historical simulations (externally forced variability). For FWC, variability in the control run exceeds that in the historical ensemble by approximately 40–45%, indicating that freshwater redistribution is strongly influenced by internal processes such as wind-driven circulation changes, ice–ocean feedbacks, and basin-scale storage variability (*25,26*). By contrast, AWCT variability is of similar magnitude in the control and historical runs, suggesting that Atlantic inflow temperature fluctuations are impacted by natural variability even in the presence of external forcing. SIA exhibits the clearest forced response: SIA variability in the historical simulations is nearly twice that in the control run at pan-Arctic scales, reflecting the strong sensitivity

of sea ice to anthropogenic warming (*27,28*). Thus, external forcing may act more as a trigger than a sustained driver, so that even removing all anthropogenic influences might have little effect on the long-term, multi-decadal trend.

To assess the role of natural variability, trends in the control runs were calculated using a 65-year running window (matching the historical simulations) and used to derive cumulative distribution functions (CDF, **Extended Data Fig. 5**), against which ensemble-mean trends from the historical runs were compared to evaluate if they exceed natural fluctuations. The AWCT trends from the historical runs lie close to the median of the control-run CDFs, indicating that the simulated long-term warming remains largely within the range of internal variability. In contrast, while historical FWC long-term trends are near the control median for the pan-Arctic and EB, the AB FWC trends exceed the 80th percentile of the control distribution, suggesting a high likelihood of an externally forced signal there. Historical runs show strongly negative SIA trends, with basin-wide means well separated from the control-run median, indicating sea ice decline far beyond natural variability and confirming a robust, forced signal.

Quantifying forced and natural contributions to atlantification events

Does external forcing make Atlantification events more intense, either in rate or amplitude? The following analysis provides a probabilistic framework for separating externally-forced or modulated contributions from naturally-driven contributions to atlantification-related events at different timescales (modes). Specifically, we consider EB FWC declines associated with halocline weakening, AWCT increases in both the AB and EB, and EB SIA declines that are potentially linked to atlantification. Corresponding slopes, defined as `trends' over respective segments of the modal time series, are calculated from the historical simulations, averaged, and compared with similar estimates of trends from the control run.

Figure 4 contrasts the strength of externally forced and naturally driven slopes in FWC, AWCT, and SIA across interannual, decadal, and multidecadal timescales. Results are averaged over all identified atlantification-related events and evaluated against observations. In addition to slope analysis, we assessed ranges defined as the differences in FWC, AWCT, and SIA values between the terminal (maximum and minimum) points of the respective modal time-series segments, yielding very similar results (**Extended Data Fig. 6**). In the EB, industrial-era FWC losses are comparable to natural variability

on interannual and decadal timescales but increase sharply on multidecadal scales, exceeding natural variability by ~52%. Although bandpass filtering may underestimate the magnitude of these multidecadal fluctuations, the main conclusion is unchanged: externally-forced multidecadal variability dominates.

By contrast, at interannual timescales, AWCT slopes from historical and control simulations are nearly identical, differing by less than ~10%, indicating a dominant role for natural variability. On decadal timescales, natural variability exceeds externally forced variability by ~30–50%, whereas on multidecadal timescales externally forced variability in the EB becomes dominant, with industrial-era slopes exceeding ~80% higher than those from control-run.

In the EB, simulated SIA slopes modulated by external forcing exceed natural variability on both decadal and multidecadal timescales, with historical-run slopes approximately 1.5–2 times larger than those from control runs. However, their systematically larger magnitude relative to observations suggests that the model overestimates sea-ice sensitivity to atmospheric forcing.

Overall, the results indicate that the model captures the qualitative emergence of externally forced signals with increasing timescale, but may misrepresent their relative strength. More generally, the model reproduces several key aspects of the modal structure of variability, although notable differences remain. In the historical simulations, AWCT and FWC variability tends to be more persistent, with relatively enhanced power at decadal and multidecadal timescales, yielding spectra that are redder than observed (**Extended Data Fig. 7**). This behavior likely reflects stronger oceanic memory and/or overly diffusive vertical mixing, which dampens high-frequency variability while amplifying low-frequency responses. At the same time, the model underestimates AWCT variability in the AB across all bands, with slopes only ~30–50% of observed magnitudes, reflecting a known deficiency in representing AW inflow and its variability into the AB (e.g., *24,29*). Despite these biases, notable similarities in spectral scaling emerge: for EB SIA across all frequencies, and for AWCT at decadal and longer timescales, simulated and observed spectra are approximately parallel, indicating comparable scaling behavior and suggesting that the governing processes controlling variance distribution across these bands are realistically represented. Thus, while the model misallocates variance across timescales and underestimates some regional processes, it nonetheless captures important

aspects of the dynamical structure and scaling of Arctic variability. These findings reinforce the view that anthropogenic forcing governs the long-term trajectory of large-scale Arctic change, while natural variability remains critical in shaping the timing, duration, and regional—particularly in the EB—expression of individual atlantification events.

Spatial patterns of atlantification events

Figure 5 shows the spatial patterns of FWC, AWCT, and SIA associated with the interannual, decadal, and multidecadal timescales, highlighting the role of atlantification in Arctic variability and verifying that the slopes used in the previous probabilistic analysis are atlantification-driven. For comparison, we use (1) ensemble-mean regression maps of water-transport time series onto FWC, AWCT, and SIA and (2) composite maps averaged over peak atlantification years in the modal time series from historical simulations (when AWCT is maximal and FWC and SIA are minimal). FWC and AWCT regression maps based on Fram Strait transports show clear advective patterns (**Extended Data Fig. 8**); similarity between these and the composite maps—quantified by pattern correlations in **Fig. 5**—therefore indicates atlantification-driven anomalies. In contrast, SIA regression patterns are not advective, characterized by weak similarity/correlation pointing to variability dominated by local processes. This is probably expected, since SIA changes driven by atlantification result from local vertical AW heat fluxes modulated by stratification changes.

The decadal and multidecadal modes exhibit spatial patterns of salinification and warming driven by advection of warm, saline waters from the subarctic seas, highlighting the role of atlantification at longer timescales. The Beaufort Gyre's expansion and contraction under atmospheric forcing may potentially contribute to atlantification patterns (e.g., *30*). By contrast, at interannual timescales, salinification and warming in the EB are not advective but reflect local freshwater redistribution and changes in AWCT, likely linked to suppressed ventilation of the AW layer. This is consistent with (*26*), who showed that interannual Arctic FWC variability is largely controlled by Pacific inflow and river discharge. Differences between locally and remotely driven FWC and AWCT changes are further supported by cross-correlations between observed AWCT, FWC, and sea ice concentration (SIC)—largely in phase at interannual scales and increasingly lagged at lower frequencies (**Extended Data Fig. 9**).

In contrast to the regression patterns, composite maps of SIC reveal clear advective-like (atlantification) structures at decadal and multidecadal scales, driven by interactions with the ocean interior. During periods of higher AW temperatures and weaker stratification, these interactions enhance sea ice loss, reflected in statistically significant correlations between SIC and AWCT (R = –0.52 and –0.65, $p < 0.05$) and between SIC and FWC (R = 0.35 and 0.59, $p < 0.05$) at decadal and multidecadal scales, respectively. By contrast, at interannual timescales, SIC patterns show no meaningful correlation with AWCT or FWC, indicating that shorter-term variability is dominated by local atmospheric processes. These results highlight that multidecadal and decadal Arctic sea ice variability is closely linked to ocean-driven processes, whereas interannual fluctuations are largely independent of AW temperatures and freshwater content.

Discussion

Observations and model simulations reveal sharply contrasting trajectories among Arctic Ocean basins in freshwater/stratification, AW temperature, and sea ice change. Since the late 1970s, the EB has experienced sustained freshwater loss and halocline weakening, whereas the AB has freshened and become more strongly stratified. These tendencies intensified during the 2000s. However, more recent (2020s) observations indicate a partial recovery of stratification in the EB, while the AB has undergone rapid freshwater loss. These recent changes coincide with a coherent decline in AWCT in both basins, marking a departure from the persistent warming observed in earlier decades and consistent with large-scale propagation of Atlantic inflow anomalies along boundary currents. The contrasting basin responses imply that similar AW anomalies can produce markedly different impacts on sea ice. This is evident in the divergent September SIA trends: the EB has continued to experience steady ice loss, whereas the decline in the AB slowed after ~2007, likely due to insulation of oceanic heat by accumulated freshwater. The persistence of reduced ice cover despite weakening AW forcing highlights the importance of halocline strength and freshwater stratification as regulators of upper-ocean ventilation and sea-ice recovery.

Analysis separating externally forced changes from natural variability shows that long-term trends linked to greenhouse radiative forcing set the evolving background state of pan-Arctic FWC, AWCT, and SIA, with particularly strong and statistically significant correlations between SIA variability and greenhouse radiative forcing ($R > 0.9$, $p <$

0.0001; **Fig. 2**). These SIA trends clearly exceed the range of natural variability, confirming a robust forced decline and underscoring the high sensitivity of sea ice to anthropogenic warming. In contrast, FWC and AWCT retain substantial natural variability, except for FWC in the AB, where the trend indicates a strong externally forced signal. Probabilistic analyses further show that internal variability contributes substantially at shorter timescales, modulating the timing and amplitude of atlantification events. Consistent with this interpretation, the observed recent partial recovery of stratification in the EB reflects internally driven decadal variability associated with shifts in oceanic circulation pathways and freshwater redistribution. These changes, however, occur against a background of persistently weakened halocline structure relative to pre-1990 conditions, allowing oceanic heat to continue influencing sea ice even during periods of reduced AW warming.

The emerging picture is one of a nonlinear, state-dependent Arctic system. atlantification should not be interpreted as a monotonic intensification of AW inflow, but rather as a series of processes that waxes and wanes in response to the balance between oceanic heat transport, freshwater accumulation, and vertical mixing. The recent increase in stratification in the EB suggests a temporary stabilization phase; however, continued upper-ocean ventilation in the EB and its eastward propagation along the Siberian slope (**Fig. 1**, *31*)—associated with ongoing sea ice decline—demonstrate that the system remains highly sensitive to oceanic forcing. In this context, the EB acts as a primary gateway through which Atlantic heat and salt influence the Arctic climate system (*1,32*). These findings imply that partial recovery of stratification alone is insufficient to reverse sea ice loss once critical thresholds in the ocean–ice coupling have been crossed. As anthropogenic forcing persists, future variability is therefore likely to be characterized by alternating periods of apparent stabilization and renewed atlantification, rather than a return to pre-2000 conditions.

Acknowledgments. This research was supported by NSF grant #1724523 (IP, AP, ML), ONR grant # N00014-21-1-2577 (IP, TB), NASA grant 80NSSC25K7431 (IP, AP), and DOE grant #280253 (IP, AP, TB, SM). This publication is partially funded by the Cooperative Institute for Climate, Ocean, & Ecosystem Studies (CICOES) under NOAA Cooperative Agreement NA20OAR4320271, Contribution No.: 2026-1547 (IP, AP). This research used resources of the National Energy Research Scientific Computing Center (NERSC), a Department of Energy User Facility using NERSC award m4968-ERCAP0036781. We thank W. Weijer for helpful discussion, comments, and suggestions.

Author Contributions. All authors contributed to data processing and preliminary analysis. AP and IP conducted statistical analyses of mooring data from the eastern Eurasian Basin. SM analyzed spatial patterns of simulated parameters, and ML analyzed synthetic time series. TB contributed to the synthesis of multidisciplinary data, while MV assisted in interpreting modeling results. All authors contributed to data interpretation and the writing of the manuscript.

Competing Interests Statement. The authors declare no competing financial interests. Correspondence and requests should be addressed to IP (ivpolyakov@alaska.edu).

Data and materials availability: The ERA5 reanalysis data is available from https://cds.climate.copernicus.eu/cdsapp#!/home. (10.24381/cds.f17050d7). CTD data prior 2017 are available online via Pangaea Data Publisher (e.g., https://doi.org/10.1594/PANGAEA.691332). 2018-2025 CTD data are available upon request. The ITP data were collected and made available by the Ice-Tethered Profiler Program (Krishfield et al., 2008) based at the Woods Hole Oceanographic Institution (http://www.whoi.edu/itp). Sea ice concentration data are available online https://www.metoffice.gov.uk/hadobs/hadisst/. Atmospheric radiative forcing data are available online https://data.giss.nasa.gov/modelforce/.

References

1. I. V. Polyakov, et al., Greater role for Atlantic inflows on sea-ice loss in the Eurasian Basin. *Science* **356**, 285–291 (2017).
2. I. V. Polyakov, R. B. Ingvaldsen, A. V. Pnyushkov, U. S. Bhatt, F. A. Francis, M. Janout, R. Kwok, Ø. Skagseth, Fluctuating Atlantic inflows modulate Arctic Atlantification. *Science* **381**, 972–979 (2023).
3. R. B. Ingvaldsen, et al., Physical manifestations and ecological implications of Arctic Atlantification. *Nat. Rev. Earth Environ.* **2**, 874–889 (2021).
4. S. Manabe, R. J. Stouffer, Sensitivity of a global climate model to an increase of CO_2 concentration. *J. Geophys. Res.* **85**, 5529–5554 (1980).
5. M. Rantanen, et al., The Arctic has warmed nearly four times faster than the globe since 1979. *Commun. Earth Environ.***3**, 168 (2022).
6. IPCC, *Climate Change 2022: Impacts, Adaptation, and Vulnerability* (Cambridge Univ. Press, 2022).
7. R. Kwok, Arctic sea ice thickness, volume, and multiyear ice coverage. *J. Geophys. Res. Oceans* **123**, 169–187 (2018).
8. J. Stroeve, D. Notz, Changing state of Arctic sea ice across all seasons. *Environ. Res. Lett.* **13**, 103001 (2018).
9. F. Vermassen, et al., Arctic sea ice during the Last Interglacial. *Nat. Commun.* **14**, 1098 (2023).
10. Q. Wang, Q. Shu, S. Wang, A. Beszczynska-Moeller, S. Danilov, L. de Steur, T. W. N. Haine, M. Karcher, C. Lee, P. G. Myers, I. V. Polyakov, C. Provost, Ø. Skagseth, G. Spreen, R. Woodgate, A review of heat and freshwater fluxes through Arctic Ocean gateways: Past changes, mechanisms, and future projections. *Ocean-Land-Atmosphere Res.*, 2, 0013, doi: 10.34133/olar.0013, (2023).
11. V. Ivanov, et al., Arctic Ocean heat impact on sea ice decline. *Geophys. Res. Lett.* **43**, 8104–8112 (2016).
12. I. V. Polyakov, T. P. Rippeth, I. Fer, M. B. Alkire, T. M. Baumann, E. C. Carmack, R. Ingvaldsen, V. V. Ivanov, M. Janout, S. Lind, L. Padman, A. V. Pnyushkov, R. Rember, Weakening of cold halocline layer exposes sea ice to oceanic heat in the eastern Arctic Ocean. *J. Clim.* **33**, 8107–8123 (2020b).

13. I. V. Polyakov, et al., Long-term variability of Arctic climate. *J. Clim.* **16**, 2078–2085 (2003a).
14. I. V. Polyakov, et al., Arctic Ocean freshwater changes. *Geophys. Res. Lett.* **30**, 1348 (2003b).
15. R. V. Bekryaev, I. V. Polyakov, V. A. Alexeev, Role of polar amplification in long-term surface air temperature variations and modern Arctic warming. *J. Clim.* **23**, 3888–3906 (2010).
16. C. Sweeney, et al., Emergent constraints on Arctic amplification. *Nat. Clim. Change* **13**, 769–776 (2023).
17. D. W. J. Thompson, J. M. Wallace, The Arctic Oscillation signature in wintertime geopotential height and temperature fields. *Geophys. Res. Lett.* **25**, 1297–1300 (1998).
18. M. Visbeck, et al., The North Atlantic Oscillation: Past, present, and future. *Proc. Natl. Acad. Sci. U.S.A.* **98**, 12876–12877 (2002).
19. D. B. Enfield, A. M. Mestas-Nuñez, P. J. Trimble, The Atlantic multidecadal oscillation and its relation to rainfall and river flows in the continental U.S. *Geophys. Res. Lett.* **28**, 2077–2080 (2001).
20. IPCC, *Climate Change 2021: The Physical Science Basis* (Cambridge Univ. Press, 2021).
21. C. Deser, A. S. Phillips, I. R. Simpson, et al., Isolating the evolving contributions of anthropogenic aerosols and greenhouse gases: A new CESM1 large ensemble community resource. *J. Clim.* **33**, 7835–7858 (2020).
22. N. C. Swart, et al., Internal variability and Arctic sea ice trends. *Geophys. Res. Lett.* **42**, 973–982 (2015).
23. M. M. Holland, L. Landrum, Factors affecting projected Arctic surface shortwave feedback. *J. Clim.* **34**, 1015–1037 (2021).
24. C. Heuzé, et al., Arctic Ocean hydrography in CMIP6 models. *J. Clim.* **36**, 1231–1252 (2023).
25. B. Rabe, et al., Arctic Ocean freshwater variability and trends. *J. Geophys. Res. Oceans* **116**, C11015 (2011).
26. A. Proshutinsky, R. Krishfield, J. M. Toole, M.-L. Timmermans, W. Williams, S. Zimmermann, M. Yamamoto-Kawai, T. W. K. Armitage, D. Dukhovskoy, E.

Golubeva, G. E. Manucharyan, G. Platov, E. Watanabe, T. Kikuchi, S. Nishino, M. Itoh, S.-H. Kang, K.-H. Cho, K. Tateyama, J. Zhao, Analysis of the Beaufort Gyre freshwater content in 2003–2018. *J. Geophys. Res. Oceans* **124**, 9658–9689 (2019).

27. J. E. Kay, et al., The influence of internal variability on Arctic sea ice trends. *Geophys. Res. Lett.* **38**, L15708 (2011).

28. Q. Ding, et al., Fingerprints of internal drivers of Arctic sea ice loss in observations and model simulations. *Nat. Clim. Change* **9**, 372–378 (2019).

29. M. Muilwijk, et al., Arctic Ocean stratification and circulation biases in CMIP6. *J. Clim.* **36**, 4789–4810 (2023).

30. J. Morison, R. Kwok, C. Peralta-Ferriz, M. Alkire, I. Rigor, R. Andersen, M. Steele, Changing Arctic Ocean freshwater pathways. *Nature* **481**, 66–70 (2012).

31. I. V. Polyakov, A. V. Pnyushkov, M. Charette, K.-H. Cho, J. Jung, L. Kipp, M. Muilwijk, L. Whitmore, E. J. Yang, J. Yoo, Atlantification advances into the Amerasian Basin of the Arctic Ocean. *Sci. Adv.* **11**, eadq7580 (2025).

32. I. V. Polyakov, M. B. Alkire, B. A. Bluhm, K. Brown, E. C. Carmack, M. Chierici, S. Danielson, I. Ellingsen, E. A. Ershova, K. Gårdfeldt, R. B. Ingvaldsen, A. V. Pnyushkov, D. Slagstad, P. Wassmann, Borealization of the Arctic Ocean in response to anomalous advection from sub-Arctic seas. *Front. Mar. Sci.* **7**, 491 (2020a).

Figure Legends

Figure 1. **Atlantification is illustrated by observed changes in Arctic Ocean circulation, stratification, and Atlantic Water (AW) properties along the Siberian slope.** (A) Schematic of sea ice drift and upper-ocean circulation (blue arrows), and AW circulation pathways (red arrows) (after *10*). Locations of oceanographic moorings MB1 and MB7 are indicated. (B-G) Mooring temperature and salinity records illustrating different stages of atlantification along the Siberian slope. (B, C) Composite monthly mean time series of water temperature (B) and the depth of the upper AW boundary, defined by the 0 °C isotherm (C), from mooring MB1. (D–G) Temperature and salinity records from the western mooring MB1 show deep (>100 m) winter ventilation, evident from winter cooling and freshening of the halocline (<50 m), superimposed on a background trend of freshening and re-stratification beginning around 2022. In contrast, the eastern mooring MB7 shows shoaling of the AW layer and no deep winter ventilation until the winter of 2025. White segments in (B-G) denote data gaps.

Figure 2. **Observations and model simulations reveal contrasting long-term changes in freshwater content (FWC), Atlantic Water core temperature (AWCT), and sea ice area (SIA) across Arctic basins.** Anomalies (relative to full time-series means) of pan-Arctic (left), Amerasian Basin (AB, middle), and Eurasian Basin (EB, right) annual mean FWC (a–f), AWCT (g–l), and September SIA (m–r). Panels a–c, g–i, and m–o show observations, with dotted lines indicating one standard error, red lines showing linear trends, and green lines showing greenhouse forcing (W m^{-2}); in panels g-i the greenhouse forcing series is divided by 2 to fit to vertical scales and in panels m-o this series is multiplied by –1. Correlations *R* between non-linear trend and greenhouse forcing time series is provided. Panels d–f, j–l, and p–r show results from the five E3SM-Arctic model runs (orange broken lines) and their ensemble means (solid red lines); also shown are observational time series smoothed with a seven-year running mean (blue lines). Trend values calculated over 1948–2025 for the observations and over 1950–2014 for the ensemble-mean historical simulations are also indicated.

Figure 3: **Arctic Ocean variability in observed FWC, AWCT, and SIA is decomposed into interannual, decadal, and multidecadal components alongside long-term trends.** FWC (a–c), AWCT (d–f), and SIA (g–i) variability decomposed into interannual, decadal, and multidecadal components, along with the long-term linear trend, for the Arctic Ocean as a whole and for the AB and EB. Standard deviations (SD) are shown using the same color scheme as the corresponding time series; the red SD represents the variability of the sum of the three components.

Figure 4: **Externally forced and natural contributions to Atlantification-related trends vary strongly with timescale, with forcing becoming dominant at longer periods.** Averaged regional trends in AWCT (°C yr^{-1}), FWC (m yr^{-1}), and SIA (10^6 km^2 yr^{-1}) illustrate AW warming in the AB and EB, halocline stratification loss in the EB, and September SIA decline in the EB. Trends are shown for three frequency bands—interannual (5–10 yr; top), decadal (15–30 yr; middle), and multidecadal (40–60 yr; bottom)—and are presented for observations (blue bars), control simulations (green bars), and industrial-era simulations (red bars). Error bars denote 95% confidence intervals.

Figure 5: Spatial patterns of atlantification show that ocean heat transport drives basin-scale changes at decadal and longer timescales, while shorter-term variability is more local. Top row: Regression coefficients of simulated Fram Strait water transport onto FWC, AWCT, and sea ice concentration (SIC), showing that increased AW inflow leads to halocline salinification and AW warming in the EB. Bottom three rows: Composite maps of FWC (m), AWCT (°C), and SIC (%) for the interannual, decadal, and multidecadal frequency bands. Composites are computed from five 1950–2014 historical simulations and averaged over the terminal phases of periods associated with halocline stratification loss, AWCT increase, and SIC decline. To emphasize advective patterns in the central Arctic, spatial means have been removed. Across the interannual, decadal, and multidecadal panels, blue shading in FWC and SIC represents freshwater and sea ice loss, respectively, whereas red shading in AWCT indicates warming. Pattern correlations *R* show connectivity between the composite and regression-based maps. Pattern correlations (*R*) highlight the connectivity between the composite and regression-based maps.

Materials and Methods

In this study, we use Arctic sea ice and oceanic datasets spanning 1948–2025, with a few exceptions. This period provides substantial overlap among key Arctic indicator time series, minimizes data gaps, and is sufficiently long to capture multiple regimes of observed variability. Data from earlier years are used to place recent changes in a broader historical context.

Sea ice data

The Met Office Hadley Centre sea ice and sea surface temperature dataset (HadISST1) provides monthly, globally complete fields of sea surface temperature (SST) and sea ice concentration on a 1° latitude–longitude grid (Rayner et al 2003). Sea ice concentrations were used to derive regional and pan-Arctic time series of sea ice area (SIA). The dataset spans the period from 1871 to the present and is constructed by combining in situ observations with satellite data and statistical interpolation to ensure spatial and temporal completeness. HadISST1 is widely used in climate studies due to its long temporal coverage and internally consistent treatment of SST and sea ice variability. The data are publicly available from the Met Office Hadley Centre (https://www.metoffice.gov.uk/hadobs/hadisst/).

Oceanic data

This study uses an updated observational archive extended to include data from 2018–2025, building on datasets previously used to investigate long-term variability in AW properties and Arctic freshwater content (e.g., Pnyushkov et al., 2022; Polyakov et al., 2008, 2013, 2018). Data coverage from 1980–2017 is illustrated by annual maps in the Supplementary Material of Polyakov et al. (2020a). The most recent additions include ship-based hydrographic observations and Ice-Tethered Profiler (ITP; www.whoi.edu/itp) measurements. The spatial and temporal coverage of the 2018–2025 data is shown in **Extended Data Fig. 10**. Together, these observations provide year-round Arctic Ocean coverage with high vertical resolution (~1 m) and high accuracy (temperature uncertainty ~0.001 °C; salinity uncertainty ~0.003 psu).

The resulting data archive provides near-continuous coverage of both the Eurasian and Amerasian basins since 1948. Although the observational record alone is insufficient to fully resolve multidecadal variability, it captures major low-frequency transitions and regime shifts. This constraint is mitigated by combining observations with long control

simulations and ensemble industrial-era model runs, which together provide the temporal context needed to separate internally-generated variability from externally-forced change.

Greenhouse radiative forcing time series

Annual time series of effective radiative forcing (ERF) at the top of the atmosphere (W m^{-2}) are taken from the NASA GISS dataset and include contributions from all forcings combined, as well as from individual components (greenhouse gases, aerosols, and natural forcings). The data span the historical period (1850–2014) and the SSP2-4.5 projection (2015–2100). All forcing estimates are referenced to a preindustrial baseline (1850). These datasets are publicly available at https://data.giss.nasa.gov/modelforce/.

Definitions

Freshwater content (FWC) is defined as the vertically integrated freshwater anomaly relative to a reference salinity of 34.8 and is expressed in meters. It represents the equivalent thickness of freshwater required to adjust the observed salinity profile to the reference value. FWC is a widely used metric for characterizing freshwater storage and stratification in the Arctic Ocean. Available potential energy (APE, e.g., Polyakov et al. 2018) provides a measure of stratification and is calculated by vertically integrating density anomalies relative to a reference state. In the EB, APE in the surface mixed layer and halocline is strongly correlated with FWC in the upper 150 m (R = 0.74–0.92; Pnyushkov et al., 2022). The model used in this study reproduces this relationship well ($R \approx 0.91$). Because FWC is simpler to compute and interpret, it is used as the primary stratification metric in this study. FWC estimates for the upper 150 m layer used here are strongly correlated ($R = 0.90$, $p < 0.0001$) with estimates referenced to the depth of the 0°C isotherm, which defines the upper boundary of the Atlantic Water layer.

AW core temperature (AWCT) is defined as the temperature maximum within the AW layer, typically located between 200 and 500 m depth. AWCT is closely related to the heat content of the Atlantic layer and is widely used as an indicator of Atlantic inflow variability (e.g., Polyakov et al. 2012).

FWC as a primary indicator of atlantification: Although AWCT is a useful diagnostic of atlantification, its surface expression depends strongly on halocline strength. Consequently, weakening of stratification—rather than warming alone—is the key

552 mechanism enabling AW heat to influence the surface ocean and sea ice. For this reason,
553 changes in FWC are emphasized as a more direct indicator of atlantification in the EB.

554 Calculating regional and pan-Arctic FWC and AWCT time series

555 Regional time series are constructed following methods used in earlier studies of Arctic
556 hydrographic variability (e.g., Polyakov et al., 2004, 2008). The Arctic Ocean is divided
557 into grid cells of 0.25° latitude × 0.75° longitude. Within each cell, observations are first
558 averaged monthly, then de-seasoned. Area-weighted averaging is subsequently applied to
559 obtain regional, annual mean time series. This approach minimizes biases associated with
560 spatially heterogeneous sampling and ensures that regions with dense observations do not
561 disproportionately influence basin-scale averages. Tests using alternative averaging
562 schemes yield nearly identical results. Regional time series from model outputs were
563 obtained by spatially averaging the relevant fields on the native model grid and weighting
564 by the local grid cell area.

565 Band-pass filtering

566 Band-pass Butterworth filters are used to isolate interannual (5–10 yr), decadal (15–30
567 yr), and multidecadal (40–60 yr) variability. Sensitivity tests using synthetic time series
568 of the same length as the observational records demonstrate that these filters effectively
569 separate the targeted frequency bands while minimizing spectral leakage. **Extended Data**
570 **Fig. 11** illustrates the filtering of a composite synthetic time series consisting of 8-, 20-,
571 and 50-yr cosine components, representing the three variability bands, together with a
572 nonlinear trend and high-frequency (<5 yr) random noise. The relative amplitudes of the
573 components are chosen to approximate their contributions to FWC variability. The results
574 confirm that the filtering successfully recovers interannual and decadal modes; however,
575 the magnitude of the multidecadal component is underestimated by approximately 30–
576 40%. Additional experiments show that when the synthetic record length matches the
577 control run (386 years), band-pass filtering successfully recovers all modes, including the
578 multidecadal.

579 Calculating lagged correlations

580 Lagged correlations between FWC, AWCT, and SIA are computed to assess temporal
581 relationships between upper-ocean stratification and subsurface heat content. Maximum
582 lags are selected based on characteristic water-mass ventilation timescales: 0–5 years for

583 the mixed layer, 5–20 years for the halocline, and 20–50 years for the AW layer. These
584 ages are typically estimated using transient tracers such as CFCs (chlorofluorocarbons)
585 and SF_6 (sulfur hexafluoride) (Schlosser et al., 1997; Tanhua et al., 2009; Smith et al.,
586 2011; Wefing et al., 2021). Statistical significance is assessed using a Student's *t*-test with
587 effective degrees of freedom estimated following Chelton (1983) to account for serial
588 autocorrelation.

589 Statistical significance and uncertainty

590 Statistical significance of trends was estimated using the Student *t* test. Statistical
591 significance of means was evaluated using the standard error (*SE*) of the mean, $SE = SD/(N_{eff})^{0.5}$, where SD is the standard deviation of the time series (sample) and N_{eff} is
593 effective sample size. N_{eff} takes into account internal correlations (or the number of
594 independent observations) and was estimated as $N_{eff} = N^*(1-R_{1ag})/(1+R_{lag})$ where N is the
595 length of the time series and R_{lag} is auto-correlation at lag = 1 (von Storch and Zwiers,
596 1999). Two *SE*s were used for evaluation of statistical significance of means at 95%
597 confidence level. Statistical significance of cross-correlations is estimated using a
598 standard Student's *t*-test, which assesses whether the observed correlation coefficients
599 differ significantly from zero, accounting for sample size and assuming normally
600 distributed data. The effective number of degrees of freedom is computed following the
601 Chelton's (1983) modified method which takes into account internal autocorrelations.

602 Wavelet analysis

603 Wavelet analysis was used to define the amplitudes and phases of the signal, which were
604 estimated using wavelet transformations of time series. The standard package of wavelet
605 programs is used for the calculation of wavelet transforms based on the DOG mother
606 function (Torrence and Compo, 1998). The 95th percentile confidence interval and cone
607 of influence shown in wavelet presentations are provided by the same package. All of the
608 time series were de-trended before the wavelet analysis. In the analysis, we used the real
609 component of the wavelet transform.

610 Model description

611 The modeling framework is based on the Energy Exascale Earth System Model (E3SM)
612 in its fully coupled, Arctic regionally refined configuration (E3SM-Arctic) as described
613 in Huo et al. (2025) and Veneziani et al. (2022, 2026). E3SM is a state-of-the-art Earth

System Model funded by the U.S. Department of Energy, consisting of component modules for the atmosphere, land, ocean, sea ice, and hydrology, connected together by a coupler component. A detailed description of the coupled model and each of its components can be found in Golaz et al. (2022), Petersen et al. (2019), Turner et al. (2022), Oleson et al. (2013) and Li et al. (2013). The model version used for the simulations analyzed in this paper is E3SMv2.1 (Smith et al. 2024, Golaz et al. 2022).

E3SM-Arctic has refined horizontal resolution in the Arctic in all model components. The atmosphere and land components share the same horizontal mesh with a resolution of 1/4° over the subarctic and mid-latitudes down to ~40°N, transitioning to 1° elsewhere on the globe. The ocean and sea ice components also share the same mesh, with horizontal resolution of 10 km over the Arctic and subpolar North Atlantic Ocean, transitioning to 30 km towards the equator and 60 km in the Southern Hemisphere. Finally, the river model has a global resolution of 1/8°. In terms of vertical resolution, E3SM-Arctic uses 72 vertical layers in the atmosphere and 80 layers in the ocean/sea ice (with a 2 m layer thickness at the surface). For this study, we utilize 6 main E3SM-Arctic simulations: a 386-year long 1950-control simulation (where GHGs were kept constant at 1950-level conditions) from which the historical ensemble was branched off, and a 5-member ensemble of fully-coupled simulations forced with historically varying levels of greenhouse gases (GHGs) covering the period 1950-2014. The control simulation provides a robust baseline for intrinsic climate variability across a wide range of timescales. The historical simulations are initialized from distinct states of the control run (January 1 of model years 101, 151, 201, 251, and 301) and are driven by time-varying natural and anthropogenic forcing. The control simulation, conducted under constant forcing, provides a baseline for internal variability. Comparing the two enables attribution of simulated changes to external forcing versus internal variability.

Model validation

Extensive comparison with observations and reanalysis products indicates that the E3SM-Arctic model realistically represents key aspects of Arctic ocean–sea ice interactions (Huo et al., 2025). In particular, the model captures large-scale thermohaline structure and air–sea coupling, but exhibits a winter warm bias associated with underestimated sea-ice area and volume. Enhanced surface albedo feedback, increased ocean heat uptake, and basal ice melt contribute to reduced ice cover and amplified surface warming. Sea ice

grows rapidly in winter but melts efficiently in summer, consistent with warmer upper-ocean temperatures. Despite biases in sea-ice thickness and volume, E3SM-Arctic provides a physically consistent framework for investigating Arctic ocean–sea ice variability (Huo et al., 2025).

Given the central role of lateral advection in atlantification, the model's representation of the boundary current along the eastern EB continental slope was evaluated using velocity observations from a cross-slope mooring array at 125°E collected during 2013–2018. The ensemble-mean of five E3SM-Arctic simulations (1950–2014) reproduces the large-scale structure of the boundary current, including the location of its core near the topographic inflection (**Extended Data Fig. 12**). Simulated core velocities (~10 cm s^{-1}) are weaker than observed (~14 cm s^{-1}), but the model captures the transition from eastward slope flow to westward offshore flow in the northern part of the section. Volume transports in both the halocline and the AW layer agree well with observations, with halocline transport differing by only ~3% (0.40 Sv versus 0.41 Sv; Pnyushkov et al., 2021). This agreement supports the suitability of E3SM-Arctic for examining advective processes associated with atlantification in the eastern EB.

Limitations of the analyses

Our analysis is limited primarily by the finite length of available observational and industrial-era model records. While these short time series may underestimate the magnitude of multidecadal signals, they do not alter our conclusion that externally forced variability dominates at multidecadal scales.

Discrepancies in reproducing the range of variability in the model simulations are consistent with known challenges in representing Arctic Ocean stratification and vertical exchange. Enhanced numerical diffusion, overly smooth haloclines, and parameterized vertical mixing modulate variability differently than observed (Heuzé et al., 2023; Muilwijk et al., 2023). Consequently, the simulated system exhibits altered variability across multiple timescales, particularly in freshwater storage and halocline recovery following perturbations.

Despite these limitations, the agreement in major tendencies between simulations and observations indicates that key processes—linking Atlantic inflows, halocline adjustment, and delayed sea-ice response—are realistically represented. Remaining discrepancies therefore primarily reflect challenges in capturing sharp stratification

gradients and long-memory processes, rather than fundamental deficiencies in representing ocean–ice interactions.

References for Methods and Extended data Figures

33. N. A. Rayner, D. E. Parker, E. B. Horton, C. K. Folland, L. V. Alexander, D. P. Rowell, E. C. Kent, A. Kaplan, Global analyses of sea surface temperature, sea ice, and night marine air temperature since the late nineteenth century. *J. Geophys. Res.* **108**, 4407 (2003).
34. A. V. Pnyushkov, G. V. Alekseev, A. V. Smirnov, On the interplay between freshwater content and hydrographic conditions in the Arctic Ocean in the 1990s–2010s. *J. Mar. Sci. Eng.* **10**, 401 (2022).
35. I. V. Polyakov, V. Alexeev, G. I. Belchansky, I. A. Dmitrenko, V. Ivanov, S. Kirillov, A. Korablev, M. Steele, L. A. Timokhov, I. Yashayaev, Arctic Ocean freshwater changes over the past 100 years and their causes. *J. Clim.* **21**, 364–384 (2008).
36. I. V. Polyakov, et al., Atlantic inflow and Arctic Ocean climate. *J. Clim.* **26**, 7052–7070 (2013).
37. I. V. Polyakov, A. V. Pnyushkov, E. C. Carmack, Stability of the Arctic halocline: A new indicator of Arctic climate change. *Environ. Res. Lett.* **13**, 125008 (2018).
38. I. V. Polyakov, A. V. Pnyushkov, L. A. Timokhov, Warming of the intermediate Atlantic Water of the Arctic Ocean in the 2000s. *J. Clim.* **25**, 8362–8370 (2012).
39. I. V. Polyakov, G. V. Alekseev, L. A. Timokhov, U. Bhatt, R. L. Colony, H. L. Simmons, D. Walsh, J. E. Walsh, V. F. Zakharov, Variability of the intermediate Atlantic Water of the Arctic Ocean over the last 100 years. *J. Clim.* **17**, 4485–4497 (2004).
40. P. Schlosser, et al., The role of large-scale Arctic Ocean circulation in the global water mass budget. *Science* **278**, 674–676 (1997).
41. T. Tanhua, E. P. Jones, E. Jeansson, Ventilation of the Arctic Ocean: Mean ages and inventories of CFC-11 and CFC-12. *J. Geophys. Res. Oceans* **114**, C01002 (2009).
42. J. N. Smith, et al., Radionuclide tracer measurements in the Arctic Ocean: Indications of recent ventilation. *Deep-Sea Res. I* **58**, 232–243 (2011).
43. A.-M. Wefing, N. Casacuberta, M. Christl, N. Gruber, J. N. Smith, Circulation timescales of Atlantic Water in the Arctic Ocean determined from anthropogenic radionuclides. *Ocean Sci.* **17**, 111–129 (2021).

44. D. B. Chelton, Effects of sampling errors in statistical estimation. *J. Atmos. Oceanic Technol.* **2**, 257–264 (1983).
45. H. von Storch, F. W. Zwiers, *Statistical Analysis in Climate Research* (Cambridge Univ. Press, 1999).
46. C. Torrence, G. P. Compo, A practical guide to wavelet analysis. *Bull. Am. Meteorol. Soc.* **79**, 61–78 (1998).
47. Y. Huo, H. Veneziani, M. Comeau, R. Osinski, B. R. Hillman, et al., E3SM-Arctic: Regionally refined coupled model for advanced understanding of Arctic system interactions. *J. Adv. Model. Earth Syst.* (2025).
48. M. Veneziani, et al., Evaluation of the E3SMv1 Arctic ocean and sea-ice regionally refined model. *Geosci. Model Dev.* **15**, 3133–3160 (2022).
49. M. Veneziani, M. Seefeldt, J. Cassano, A.-M. Strehl, Processes driving interannual variability of deep convection in the Nordic Seas. *J. Clim.*, under review (2026).
50. J.-C. Golaz, et al., The DOE E3SM model version 2: Overview of the physical model and initial model evaluation. *J. Adv. Model. Earth Syst.* **14**, e2022MS003156 (2022).
51. M. R. Petersen, et al., Evaluation of the ocean and sea ice climate of E3SM using MPAS. *J. Adv. Model. Earth Syst.* **11**, 1438–1458 (2019).
52. A. K. Turner, W. H. Lipscomb, E. C. Hunke, D. W. Jacobsen, N. Jeffery, D. Engwirda, T. D. Ringler, J. D. Wolfe, MPAS-Seaice (v1.0.0): Sea-ice dynamics on unstructured Voronoi meshes. *Geosci. Model Dev.* **15**, 3721–3751 (2022).
53. K. W. Oleson, et al., Technical description of version 4.5 of the Community Land Model (CLM). NCAR Tech. Rep. (2013).
54. H. Li, M. S. Wigmosta, H. Wu, M. Huang, Y. Ke, A. M. Coleman, L. R. Leung, A physically based runoff routing model for land surface and Earth system models. *J. Hydrometeorol.* **14**, 808–828 (2013).
55. K. M. Smith, et al., The DOE E3SM version 2.1: Overview and impacts of parameterized ocean submesoscales. *Geosci. Model Dev.* **18**, 1613–1633 (2024).
56. A. V. Pnyushkov, I. V. Polyakov, I. M. Ashik, G. V. Alekseev, T. M. Baumann, E. C. Carmack, V. V. Ivanov, R. Rember, A steady regime of volume and heat transports in the eastern Arctic Ocean in the early 21st century. *Front. Mar. Sci.* **8**, 705608 (2021).

Extended Data Figure Legends

Extended Data Figure 1: Coupled variability in the Arctic atmosphere-ice-ocean system. Time series (left, dotted lines are for annual and solid blue lines are for 7 year running means) and wavelet transforms of detrended time series of annual surface air temperature (a, SAT), fastice thickness (b, $H_{fastice}$), and Atlantic Water core temperature (c, AWCT) anomalies. In panels with wavelet transforms, the vertical axis shows period in years, 95 % statistical significance and cones of influence are shown by grey lines. Wavelets (with units of the variable divided by the square root of time) show how much power (variance) is concentrated at a certain frequency (period) and time. For example, wavelet maxima at ~50–60 years corresponds to warm regimes in the 1930s–1940s and recent decades, whereas wavelet minima at these time scales correlate to cold regimes in the early part of the record and the 1960s–1980s.

Extended Data Figure 2: Time series (a,c) of annual FWC anomalies (m) and their wavelet transforms (b,d) for the AB and EB. In the wavelet ($m/s^{0.5}$) panels, grey contours indicate the 95% significance level and the cone of influence. Linear trends computed over 1948–2025, 1999–2025, and 2019–2025 are shown by red, green, and light-blue lines, respectively, with corresponding numerical values indicated.

Extended Data Figure 3. Anomalies (relative to time series means) of pan-Arctic (left), Amerasian Basin (middle), and Eurasian Basin (right) time series of FWC (top), AWCT (middle), and SIA (bottom) from the control run (black lines, 386 years) and five historical runs (colored lines) from the E3SM-Arctic model experiments. Standard deviations (SD) from the control run and the mean of five SD estimates from the historical runs are shown.

Extended Data Figure 4: (a) Time series of pan-Arctic (AB + EB) sea ice area (SIA) anomalies (10^6 km²). (b, c) Regional SIA anomalies for the AB (b) and EB (c) during the 2007–2025 hiatus period, together with linear trends for 2007–2025 (blue) and 2007–2021 (orange). (d) Regional SIA trends computed for consecutive end years starting from 2007; the larger dot marking the 2021 EB trend denotes statistical significance at the 95% confidence level.

Extended Data Figure 5: Cumulative distribution functions of trends in annual AWCT (°C $decade^{-1}$), FWC (m $decade^{-1}$), and September SIA (10^6 km² $decade^{-1}$) derived from control runs (blue curves) and from the historical runs, shown as the mean (solid red) with associated standard errors (dotted red). Trends in the control runs are calculated using a running window with a length equal to that of the historical simulations (65 years).

Extended Data Figure 6: Averaged regional ranges of variability in FWC (m), AWCT (°C), and SIA (10^6 km²) associated with atlantification (e.g., ranges of AW warming in

the AB and EB, halocline stratification loss in the EB, and September SIA decline in the EB), shown for three frequency bands: interannual (5–10 years; top), decadal (15–30 years; middle), and multidecadal (40–60 years; bottom). Ranges are shown for observations (blue bars), the control simulation (green bars), and industrial-era simulations (red bars). Error bars denote 95% confidence intervals, with uncertainties averaged across all available estimates.

Extended Data Figure 7: Power spectra of observed (green) and simulated time series—control run (blue) and historical runs (dotted red for individual runs, solid red for ensemble-mean spectra)—for AB and EB AWCT, and EB FWC and SIA.

Extended Data Figure 8: (Top) Ensemble-mean regression maps from five industrial-era simulations of FWC (a), AWCT (b), and SIC (c) onto total water transport across Fram Strait. (d) Time series of total water transport (Sv) across Fram Strait from the five simulations (dashed gray lines) and their ensemble mean (solid blue line). (e) Anomalies of ensemble mean total water transport and its inflow component (Sv) across Fram Strait, illustrating that variability in total transport is dominated by the inflow component.

Extended Data Figure 9: Lagged correlations between FWC and AWCT (dark blue), FWC and SIA (light blue) and AWCT and SIA (red) derived from observations for three selected frequency bands: interannual 5–10 years (top), decadal 15–30 years (middle), and multidecadal 40–60 years (bottom). Statistically significant ($p < 0.05$) correlations are shown by thicker lines.

Extended Data Figure 10: Maps with locations of CTD stations (red dots) in 2018-2025.

Extended Data Figure 11: The composite synthetic time series comprises 8-, 20-, and 50-yr cosine components representing interannual (5–10 yr), decadal (15–30 yr), and multidecadal (40–60 yr) variability, respectively, together with a residual nonlinear trend approximated by greenhouse radiative forcing and high-frequency random noise approximating <5-yr timescales; both not shown; see Methods 3c. Correlation coefficients (*R*) and standard deviations (*SD*) are indicated.

Extended Data Figure 12. (A) Mean eastward velocities (cm/s) averaged over 2013–2018 from mooring observations at the Laptev Sea slope in the upper 800 m (adapted from Pnyushkov et al., 2021). Black triangles indicate mooring locations. (B) Simulated ensemble-mean zonal velocities from five historical runs for 1950–2014.

Figures

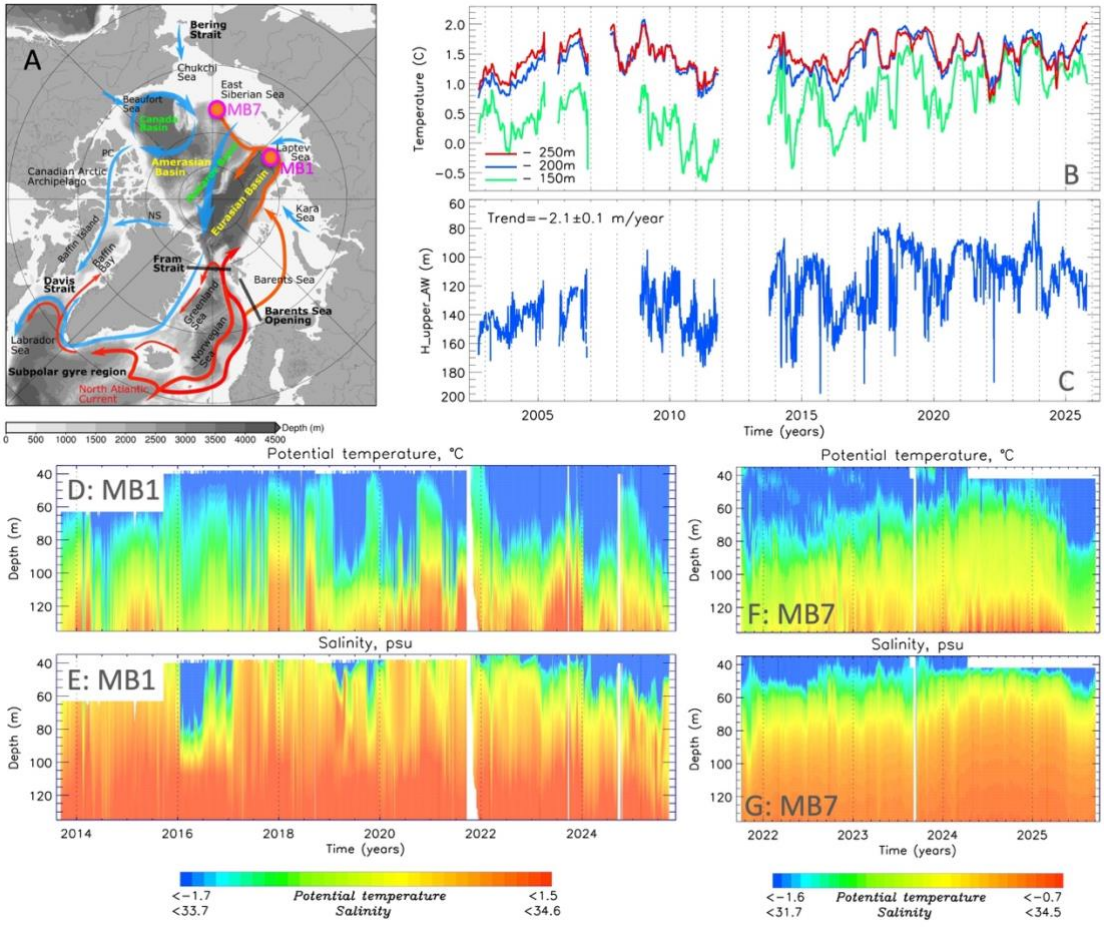


Figure 1. **Atlantification is illustrated by observed changes in Arctic Ocean circulation, stratification, and Atlantic Water (AW) properties along the Siberian slope.** (A) Schematic of sea ice drift and upper-ocean circulation (blue arrows), and AW circulation pathways (red arrows) (after *10*). Locations of oceanographic moorings MB1 and MB7 are indicated. (B-G) Mooring temperature and salinity records illustrating different stages of atlantification along the Siberian slope. (B, C) Composite monthly mean time series of water temperature (B) and the depth of the upper AW boundary, defined by the 0 °C isotherm (C), from mooring MB1. (D–G) Temperature and salinity records from the western mooring MB1 show deep (>100 m) winter ventilation, evident from winter cooling and freshening of the halocline (<50 m), superimposed on a background trend of freshening and re-stratification beginning around 2022. In contrast, the eastern mooring MB7 shows shoaling of the AW layer and no deep winter ventilation until the winter of 2025. White segments in (B-G) denote data gaps.

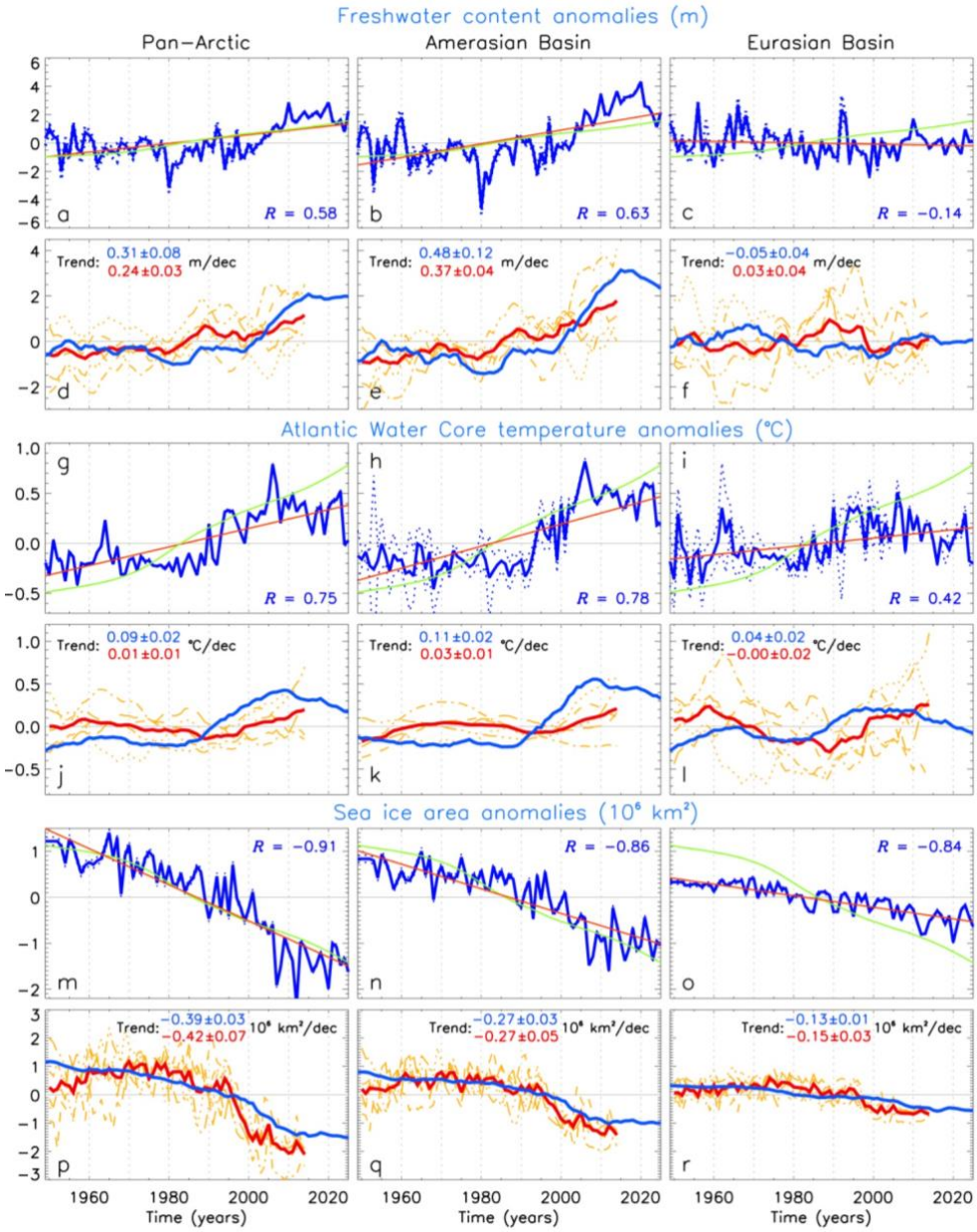


Figure 2. **Observations and model simulations reveal contrasting long-term changes in freshwater content (FWC), Atlantic Water core temperature (AWCT), and sea ice area (SIA) across Arctic basins.** Anomalies (relative to full time-series means) of pan-Arctic (left), Amerasian Basin (AB, middle), and Eurasian Basin (EB, right) annual mean FWC (a–f), AWCT (g–l), and September SIA (m–r). Panels a–c, g–i, and m–o show observations, with dotted lines indicating one standard error, red lines showing linear trends, and green lines showing greenhouse forcing (W m^{-2}); in panels g-i the greenhouse forcing series is divided by 2 to fit to vertical scales and in panels m-o this series is multiplied by –1. Correlations *R* between non-linear trend and greenhouse forcing time series is provided. Panels d–f, j–l, and p–r show results from the five E3SM-Arctic model runs (orange broken lines) and their ensemble means (solid red lines); also shown are observational time series smoothed with a seven-year running mean (blue lines). Trend values calculated over 1948–2025 for the observations and over 1950–2014 for the ensemble-mean historical simulations are also indicated.

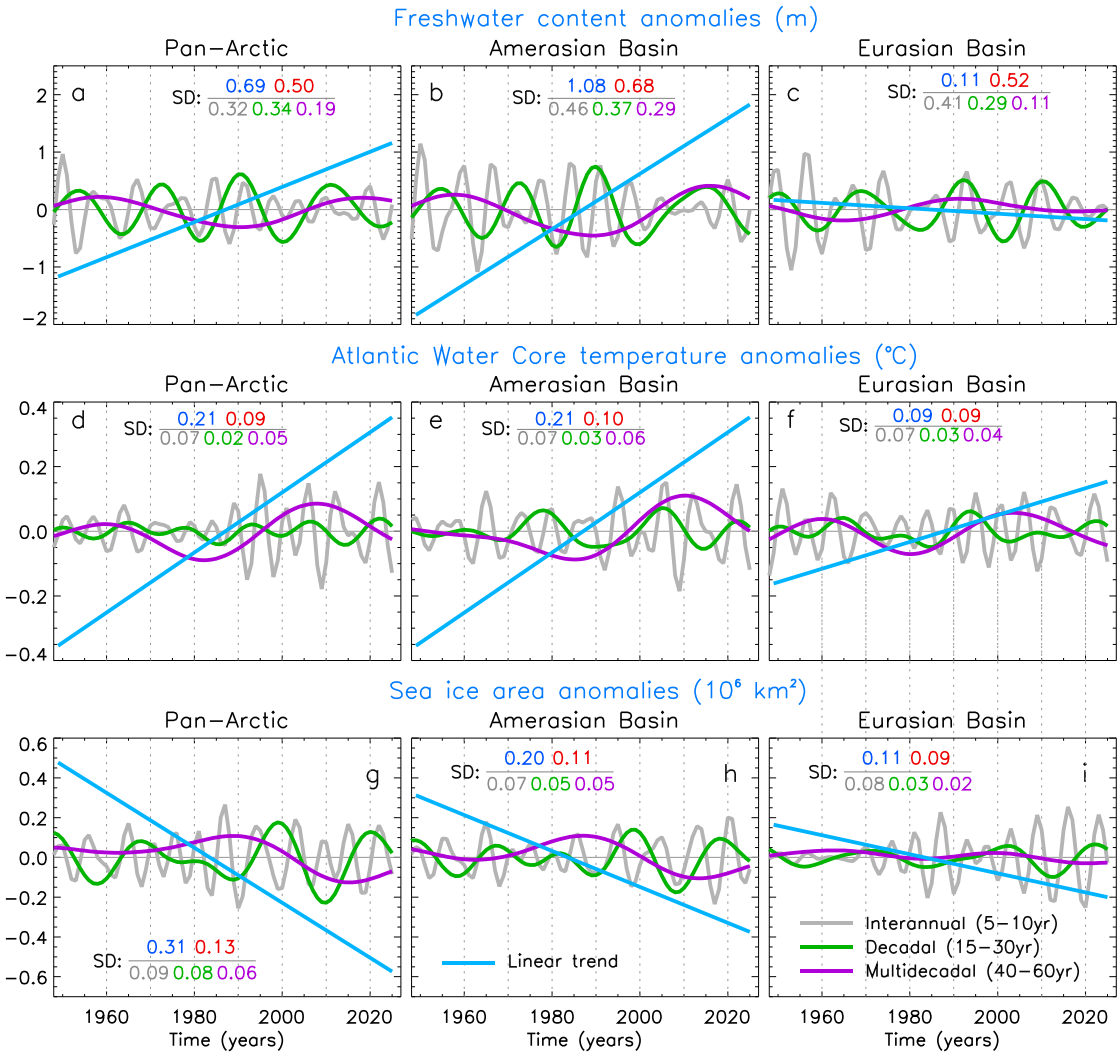


Figure 3: **Arctic Ocean variability in observed FWC, AWCT, and SIA is decomposed into interannual, decadal, and multidecadal components alongside long-term trends.** FWC (a–c), AWCT (d–f), and SIA (g–i) variability decomposed into interannual, decadal, and multidecadal components, along with the long-term linear trend, for the Arctic Ocean as a whole and for the AB and EB. Standard deviations (SD) are shown using the same color scheme as the corresponding time series; the red SD represents the variability of the sum of the three components.

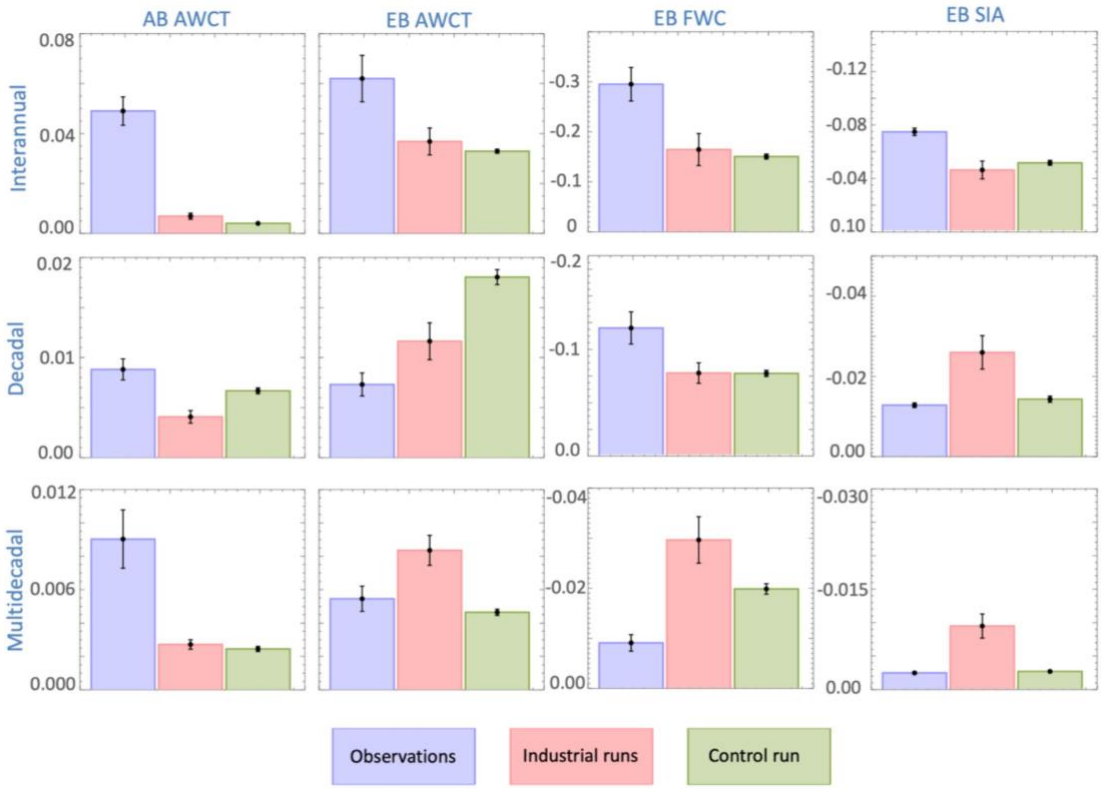
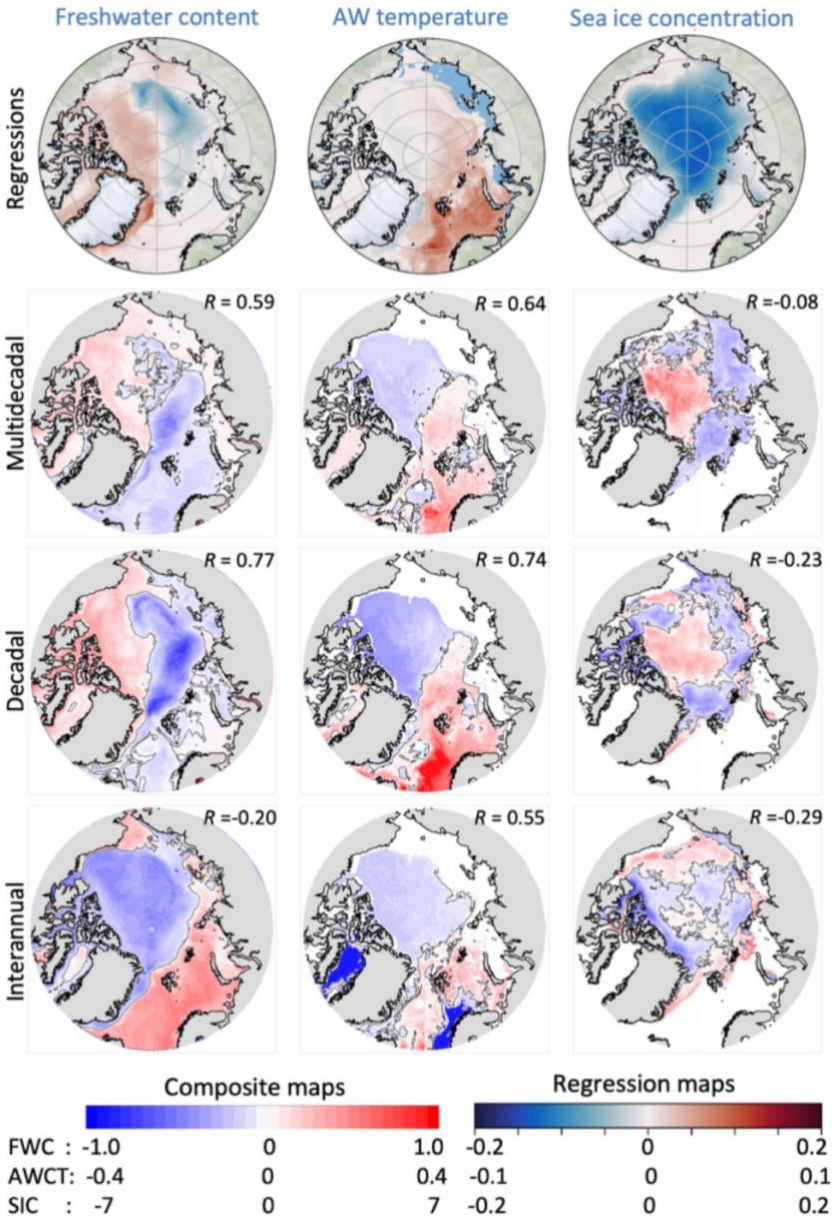


Figure 4: **Externally forced and natural contributions to Atlantification-related trends vary strongly with timescale, with forcing becoming dominant at longer periods.** Averaged regional trends in AWCT (°C yr^{-1}), FWC (m yr^{-1}), and SIA (10^6 km^2 yr^{-1}) illustrate AW warming in the AB and EB, halocline stratification loss in the EB, and September SIA decline in the EB. Trends are shown for three frequency bands—interannual (5–10 yr; top), decadal (15–30 yr; middle), and multidecadal (40–60 yr; bottom)—and are presented for observations (blue bars), control simulations (green bars), and industrial-era simulations (red bars). Error bars denote 95% confidence intervals.



873

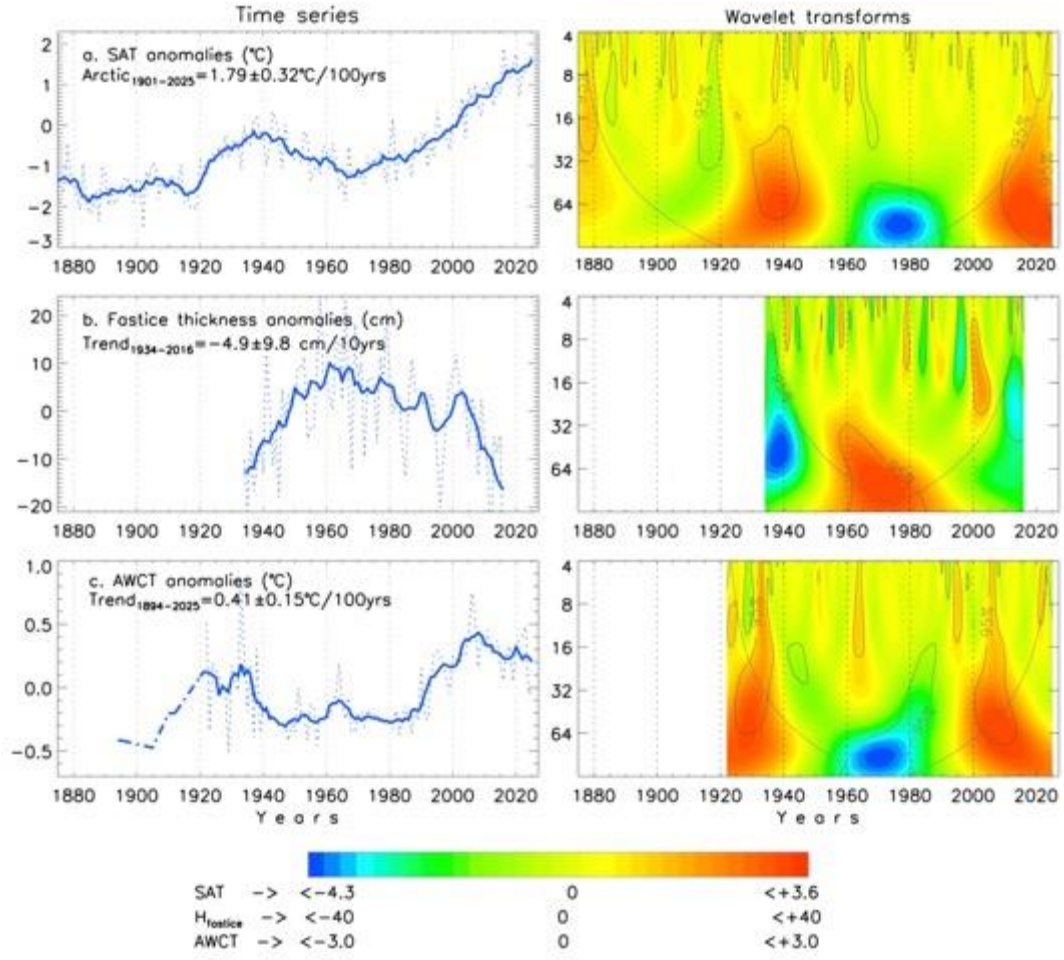
874 **Figure 5: Spatial patterns of atlantification show that ocean heat transport drives**
875 **basin-scale changes at decadal and longer timescales, while shorter-term variability**
876 **is more local.** Top row: Regression coefficients of simulated Fram Strait water transport
877 onto FWC, AWCT, and sea ice concentration (SIC), showing that increased AW inflow
878 leads to halocline salinification and AW warming in the EB. Bottom three rows:
879 Composite maps of FWC (m), AWCT (°C), and SIC (%) for the interannual, decadal, and
880 multidecadal frequency bands. Composites are computed from five 1950–2014 historical
881 simulations and averaged over the terminal phases of periods associated with halocline
882 stratification loss, AWCT increase, and SIC decline. To emphasize advective patterns in
883 the central Arctic, spatial means have been removed. Across the interannual, decadal, and
884 multidecadal panels, blue shading in FWC and SIC represents freshwater and sea ice loss,
885 respectively, whereas red shading in AWCT indicates warming. Pattern correlations *R*
886 show connectivity between the composite and regression-based maps. Pattern
887 correlations (*R*) highlight the connectivity between the composite and regression-based
888 maps.

Extended Data for

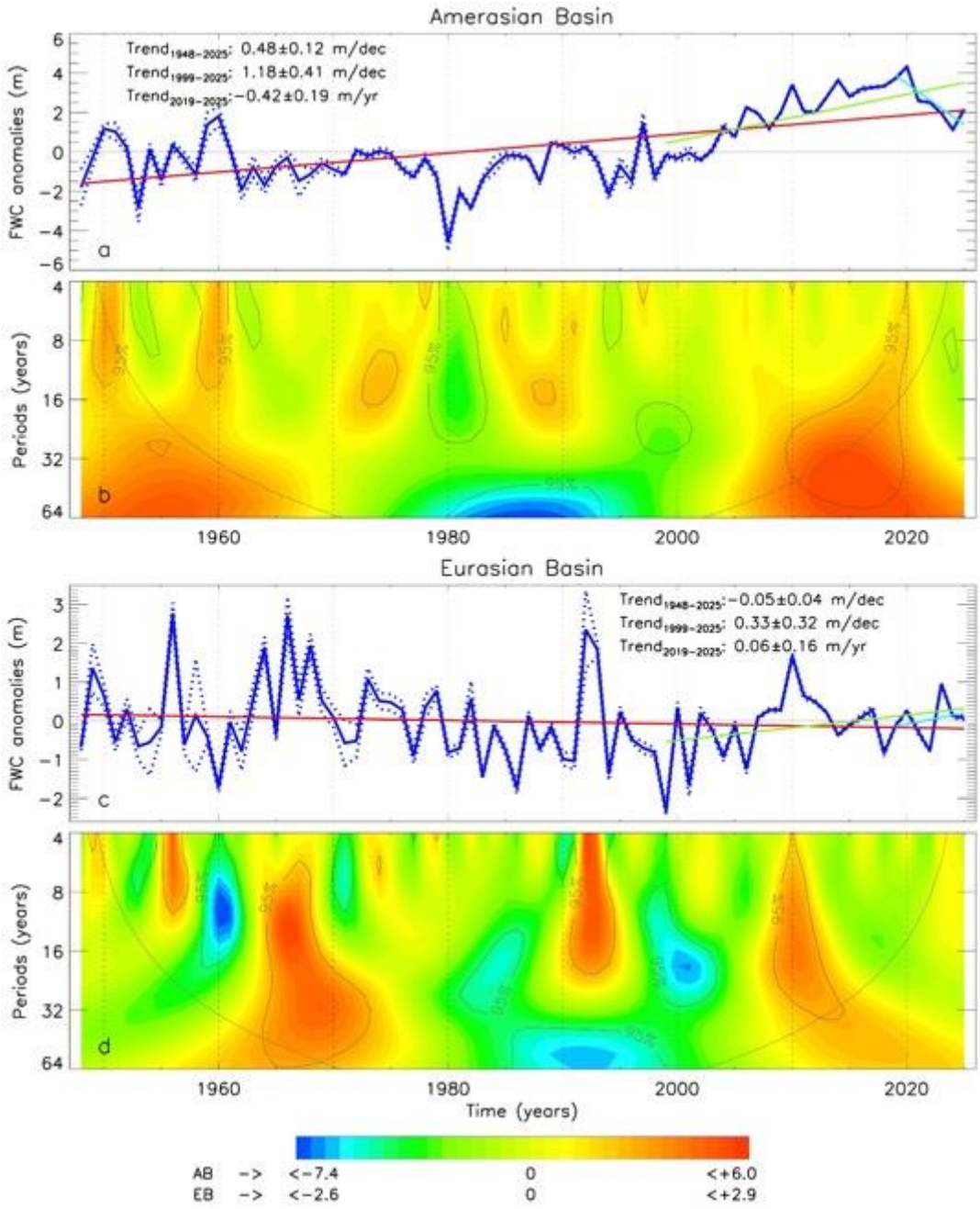
The role of natural and forced variability in shaping atlantification of the Arctic Ocean

Igor V. Polyakov, Andrey V. Pnyushkov, Thomas J. Ballinger,
Michael Lundberg, Sergey Molodtsov, Milena Veneziani

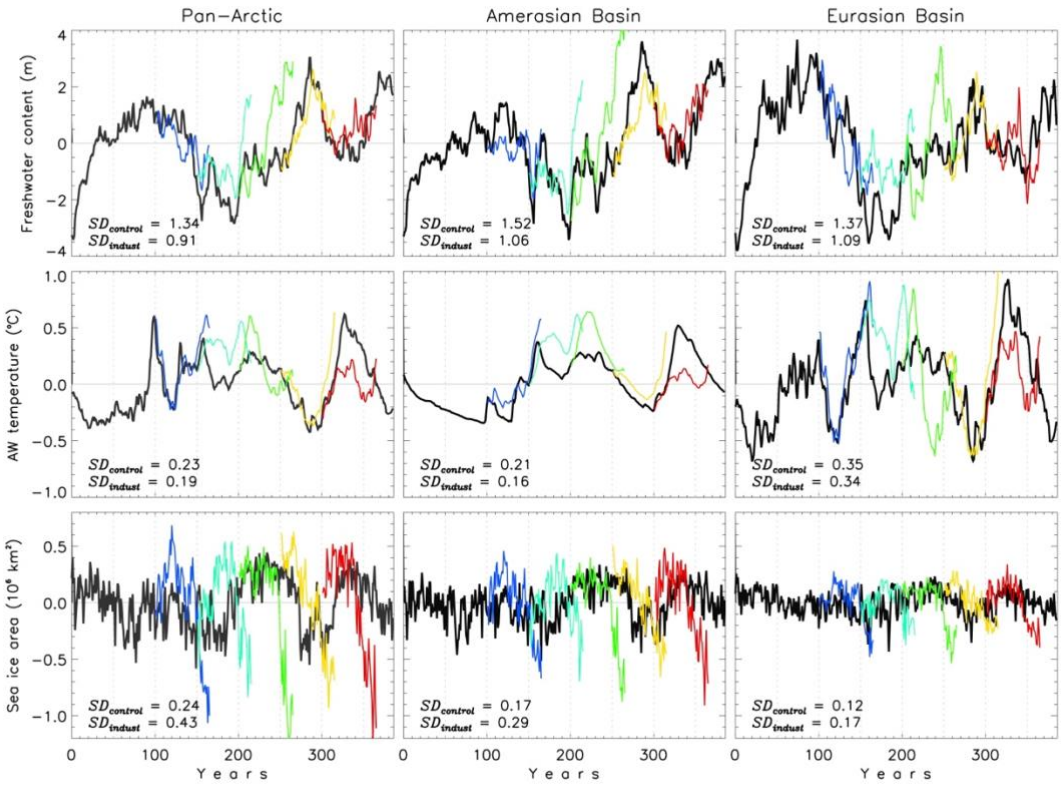
correspondence to: ivpolyakov@alaska.edu



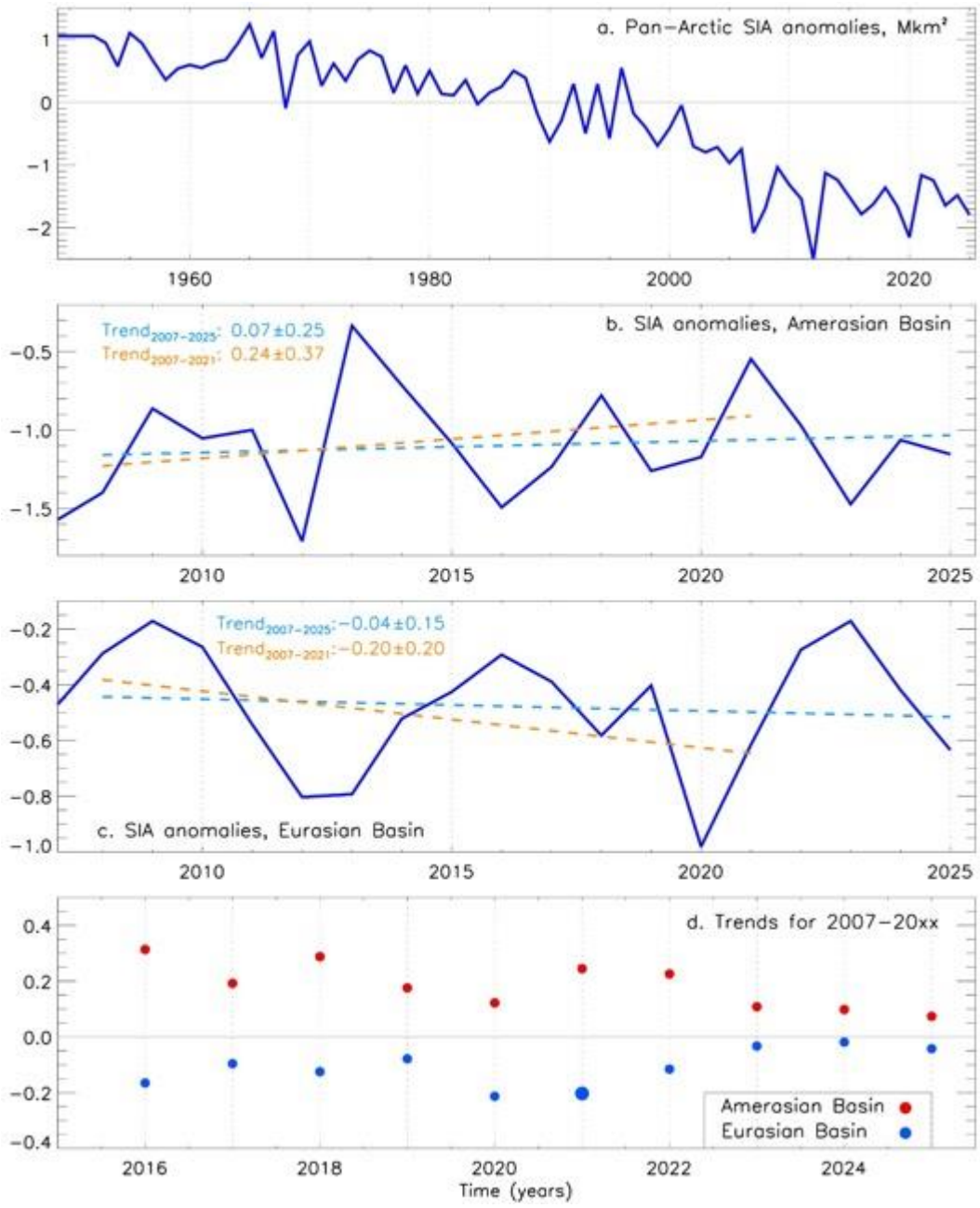
Extended Data Figure 1: Coupled variability in the Arctic atmosphere-ice-ocean system. Time series (left, dotted lines are for annual and solid blue lines are for 7 year running means) and wavelet transforms of detrended time series of annual surface air temperature (a, SAT), fastice thickness (b, $H_{fastice}$), and Atlantic Water core temperature (c, AWCT) anomalies. In panels with wavelet transforms, the vertical axis shows period in years, 95 % statistical significance and cones of influence are shown by grey lines. Wavelets (with units of the variable divided by the square root of time) show how much power (variance) is concentrated at a certain frequency (period) and time. For example, wavelet maxima at ~50–60 years corresponds to warm regimes in the 1930s–1940s and recent decades, whereas wavelet minima at these time scales correlate to cold regimes in the early part of the record and the 1960s–1980s.



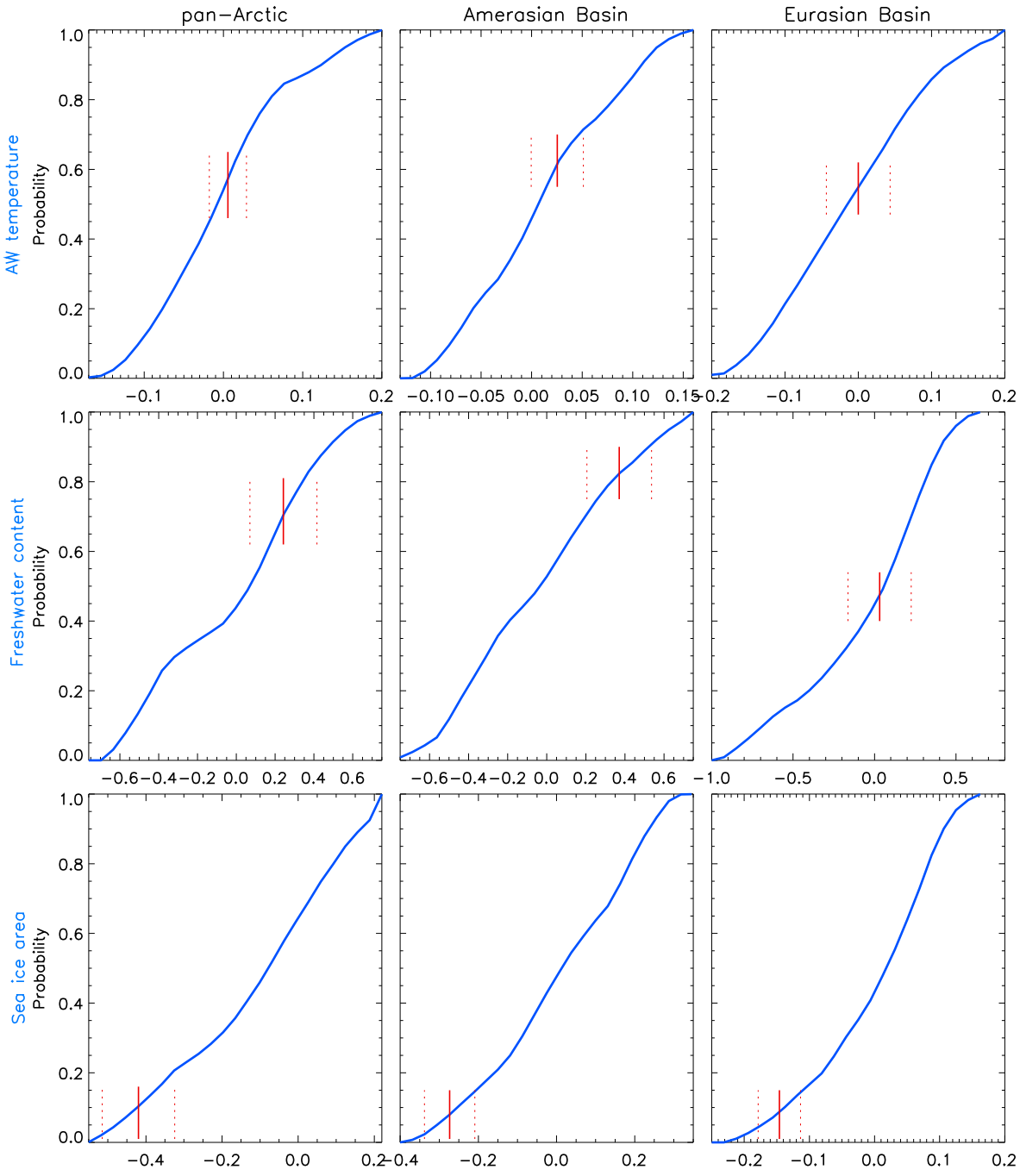
Extended Data Figure 2: Time series (a,c) of annual FWC anomalies (m) and their wavelet transforms (b,d) for the AB and EB. In (a,c), linear trends computed over 1948–2025, 1999–2025, and 2019–2025 are shown by red, green, and light-blue lines, respectively, with corresponding numerical values indicated. In (b,d) ($m/s^{0.5}$), grey contours indicate the 95% significance level and the cone of influence.



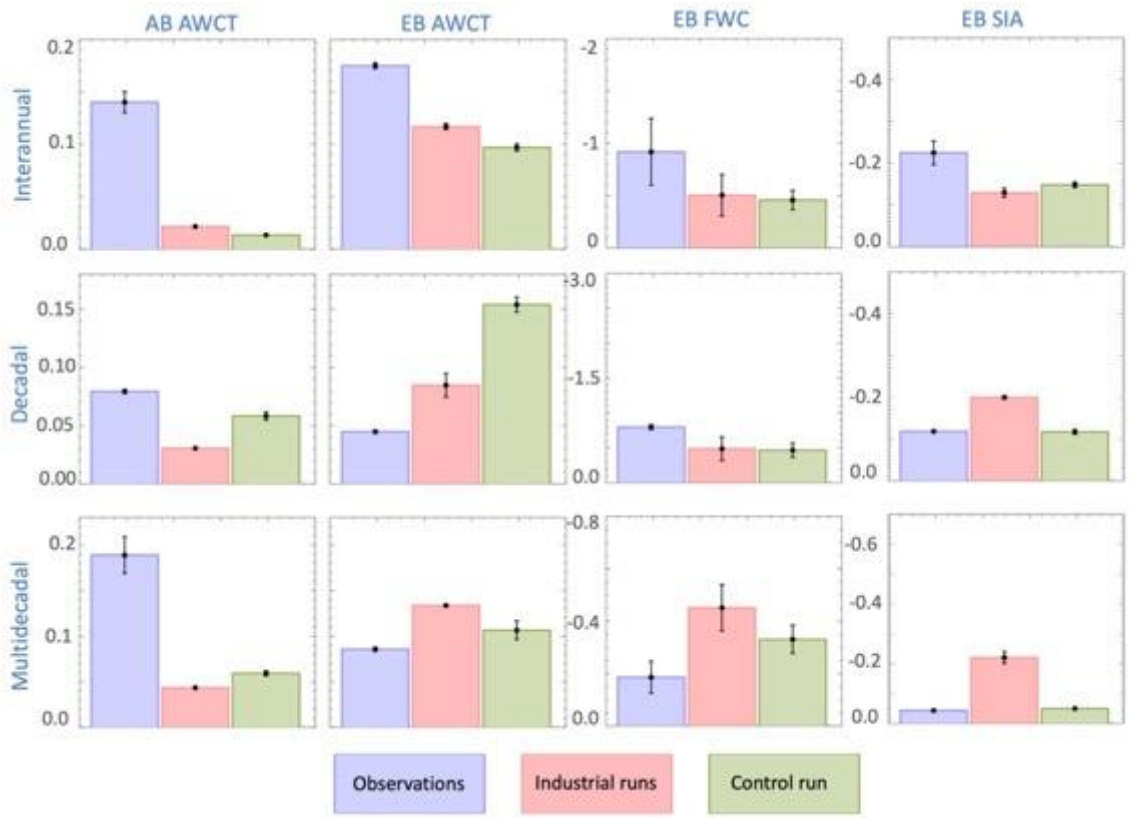
Extended Data Figure 3. Anomalies (relative to full time series means) of pan-Arctic (left), Amerasian Basin (middle), and Eurasian Basin (right) time series of FWC (top), AWCT (middle), and SIA (bottom) from the E3SM-Arctic control run (black lines, 386 years) and five historical runs (colored lines). Standard deviations (SD) from the control run (with the first 100 years excluded) and the mean of five SD estimates from the historical runs are shown.



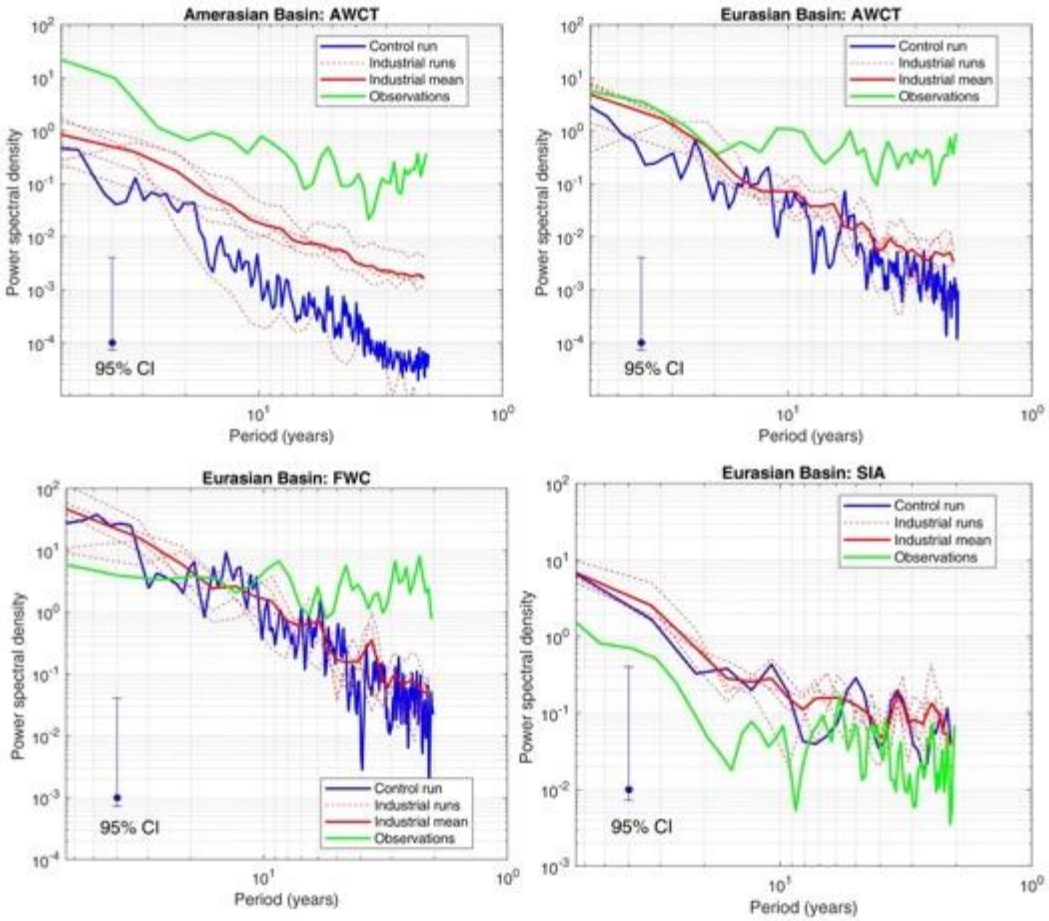
Extended Data Figure 4: (a) Time series of pan-Arctic (AB + EB) sea ice area (SIA) anomalies (10^6 km²). (b, c) Regional SIA anomalies for the AB (b) and EB (c) during the 2007–2025 hiatus period, together with linear trends for 2007–2025 (blue) and 2007–2021 (orange). (d) Regional SIA trends computed for consecutive end years starting from 2007 (e.g., 2007-2016, 2007-2017, etc.). All trends, except 2007-2021 EB trend (marked by a lagger dot), are not significant at the 95% confidence level.



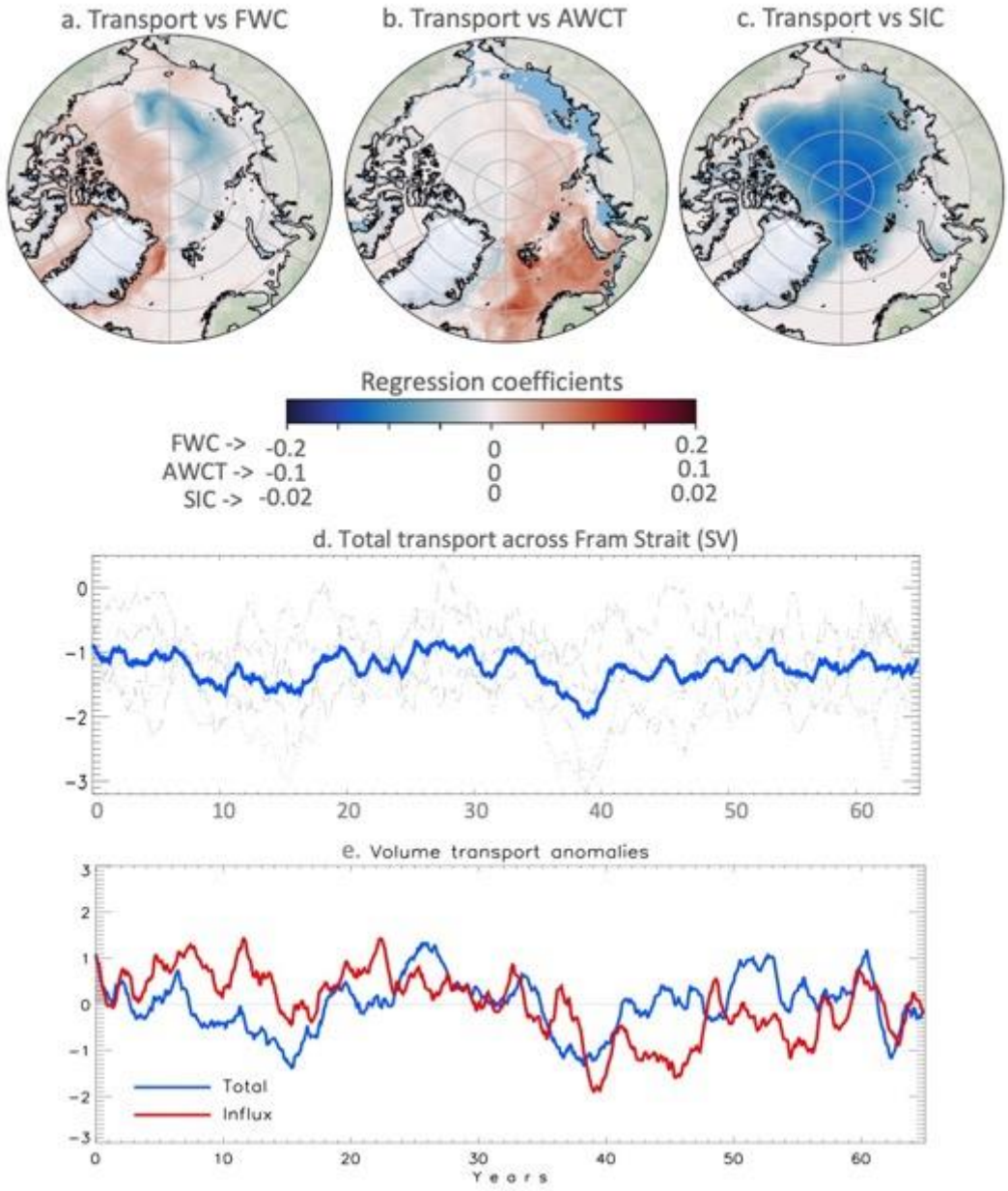
Extended Data Figure 5: Cumulative distribution functions of trends in annual AWCT (°C decade^{-1}), FWC (m decade^{-1}), and September SIA (10^6 km^2 decade^{-1}) derived from control runs (blue curves) and from the historical runs, shown as the mean (solid red) with associated standard errors (dotted red). Trends in the control runs are calculated using a 65-years running window with a length equal to that of the historical simulations (first 100 years excluded).



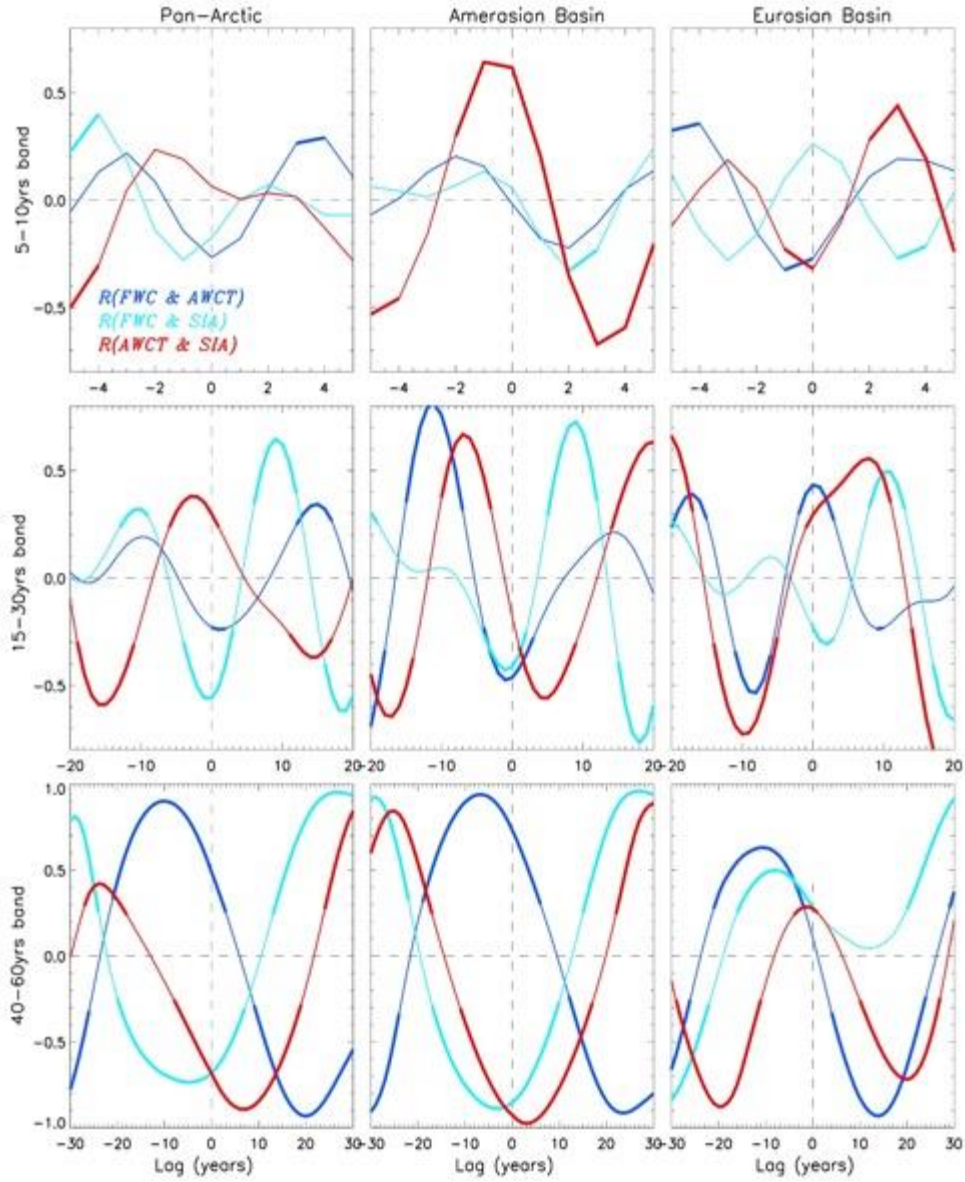
Extended Data Figure 6: Averaged regional ranges of variability in FWC (m), AWCT (°C), and SIA (10^6 km²) associated with atlantification (e.g., ranges of AW warming in the AB and EB, halocline stratification loss in the EB, and September SIA decline in the EB), shown for three frequency bands: interannual (5–10 years; top), decadal (15–30 years; middle), and multidecadal (40–60 years; bottom). Ranges are shown for observations (blue bars), the control simulation (green bars), and industrial-era simulations (red bars). Error bars denote 95% confidence intervals.



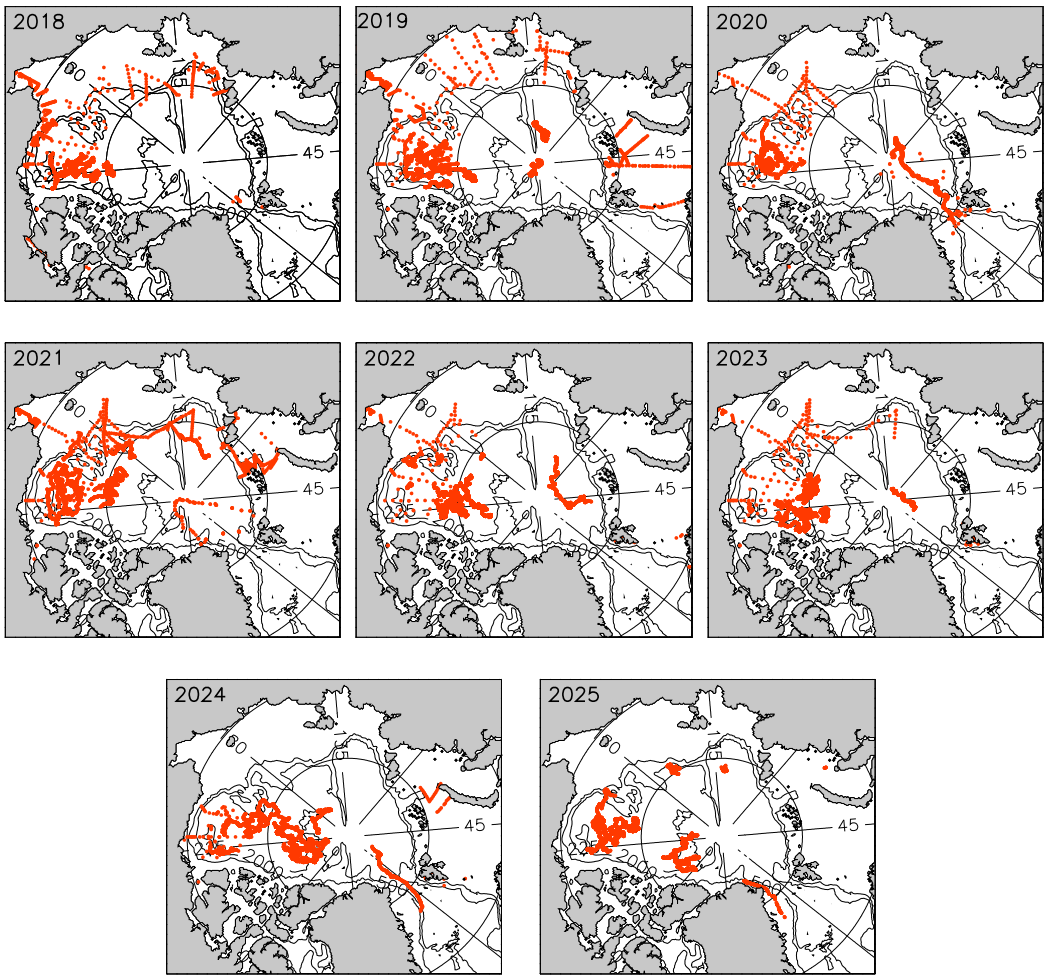
Extended Data Figure 7: Power spectra of observed (green) and simulated time series—control run (blue) and historical runs (dotted red for individual runs, solid red for ensemble-mean spectra)—for AB and EB AWCT, and EB FWC and SIA.



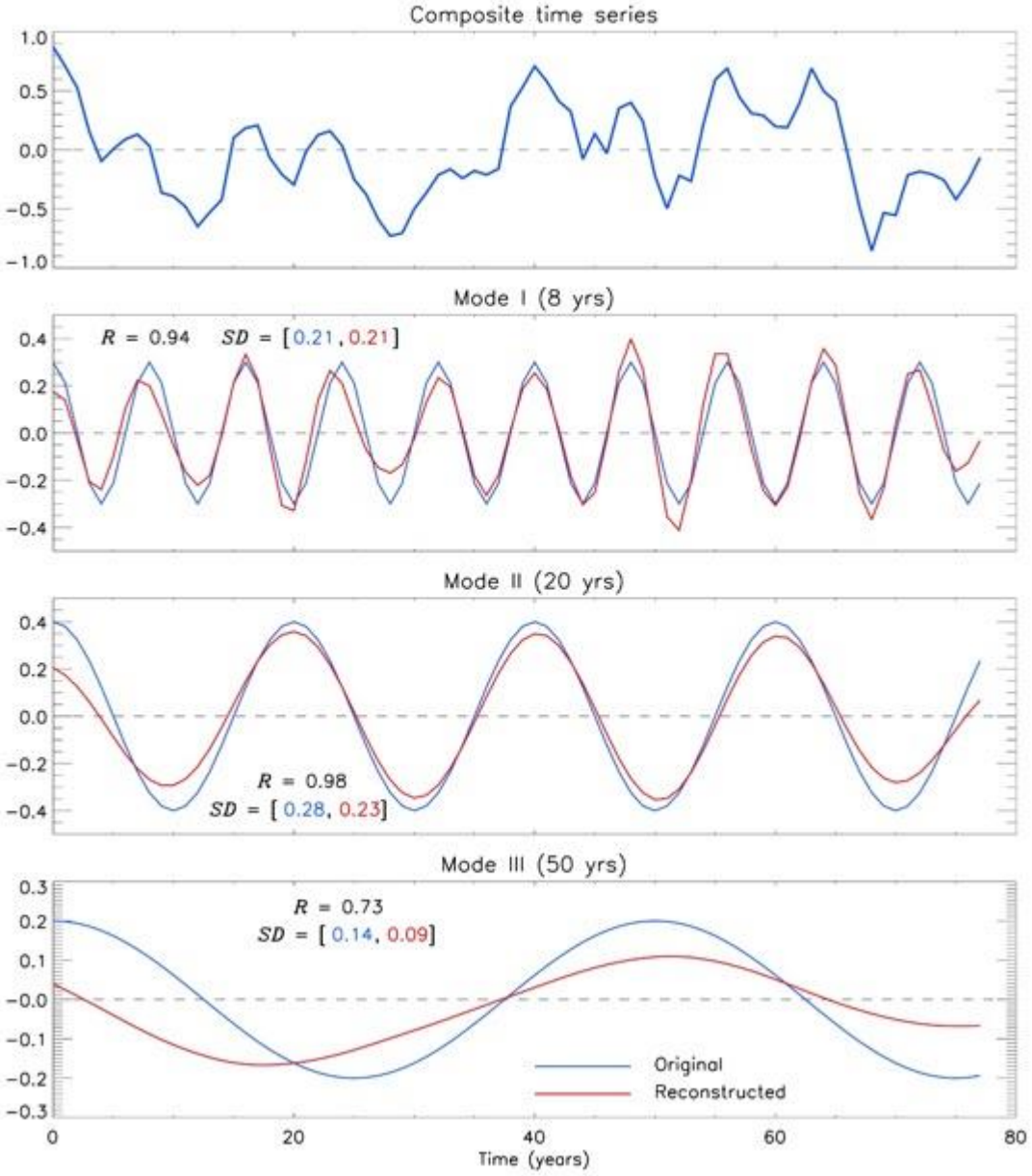
Extended Data Figure 8: (Top) Ensemble-mean regression maps from five industrial-era simulations of FWC (a), AWCT (b), and SIC (c) onto total water transport across Fram Strait. (d) Time series of total water transport (Sv) across Fram Strait from the five simulations (dashed gray lines) and their ensemble mean (solid blue line). (e) Anomalies of ensemble mean total water transport and its inflow component (Sv) across Fram Strait, illustrating that variability in total transport is dominated by the inflow component.



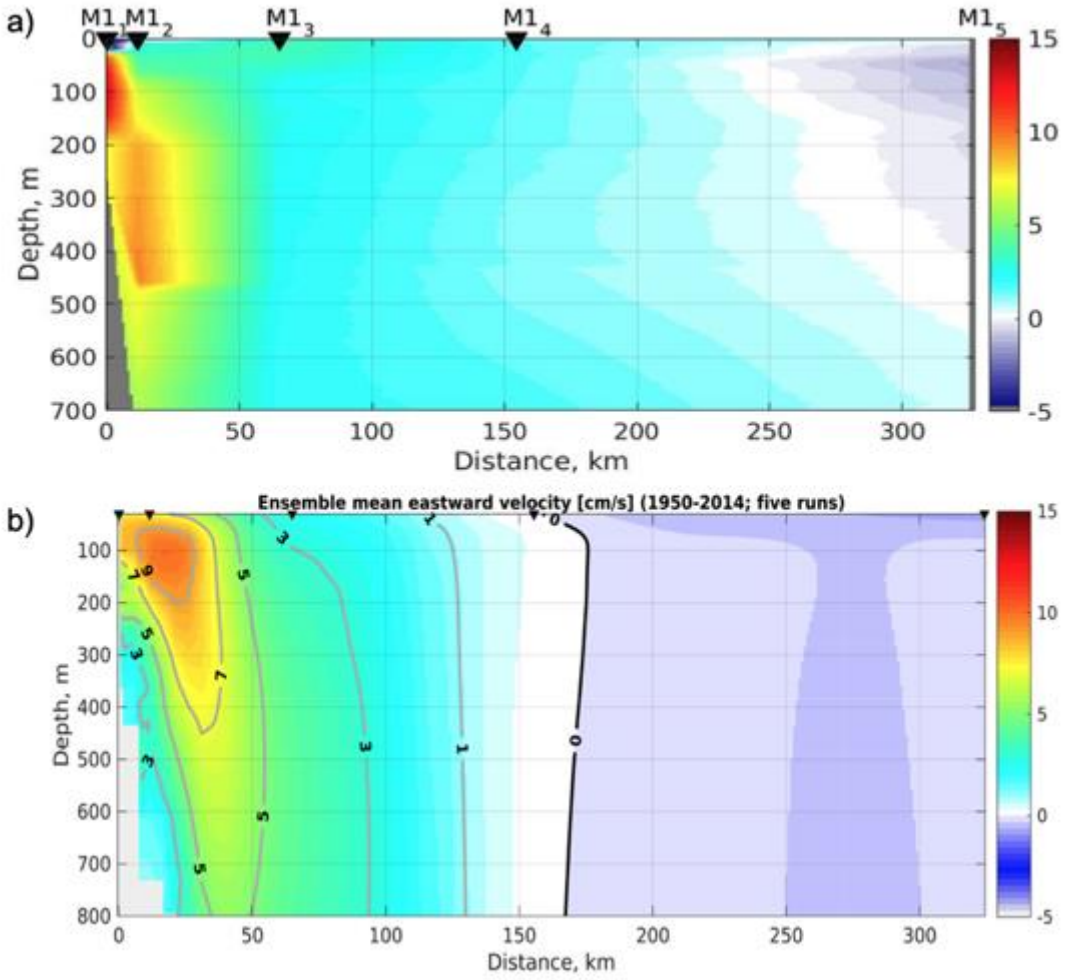
Extended Data Figure 9: Lagged correlations between FWC and AWCT (dark blue), FWC and SIA (light blue) and AWCT and SIA (red) derived from observations for three selected frequency bands: interannual 5–10 years (top), decadal 15–30 years (middle), and multidecadal 40–60 years (bottom). Statistically significant ($p < 0.05$) correlations are shown by thicker lines.



Extended Data Figure 10: Maps with locations of CTD/ITP stations (red dots) in 2018-2025.



Extended Data Figure 11: The composite synthetic time series comprises 8-, 20-, and 50-yr cosine components representing interannual (5–10 yr), decadal (15–30 yr), and multidecadal (40–60 yr) variability, respectively, together with a residual nonlinear trend approximated by greenhouse radiative forcing and high-frequency random noise approximating <5-yr timescales; both not shown; see Methods 3c. Correlation coefficients (*R*) and standard deviations (*SD*) are indicated.



Extended Data Figure 12. (A) Mean eastward velocities (cm/s) averaged over 2013–2018 from mooring observations at the Laptev Sea slope in the upper 800 m (adapted from *56*). Black triangles indicate mooring locations. (B) Simulated ensemble-mean zonal velocities from five historical runs for 1950–2014.